Electrostatic Pull-in Test Structure Design for *In-Situ* Mechanical Property Measurements of Microelectromechanical Systems (MEMS)

by

Raj K. Gupta

B.S. University of Illinois at Urbana-Champaign (December 1990)
S.M. Massachusetts Institute of Technology (June 1993)

submitted to the Department of Electrical Engineering and Computer Science
in partial fulfillment of the requirements for the degree of

Doctor of Philosophy

at the Massachusetts Institute of Technology
June 1997

© 1997 Massachusetts Institute of Technology
All rights reserved.

Signature of Author . . . .
Department of Electrical Engineering and Computer Science
May 16, 1998

Certified by . . . .
Stephen D. Senturia, Barton L. Weller Professor
Department of Electrical Engineering and Computer Science
Thesis Supervisor

Accepted by . . . .
Arthur C. Smith
Chairman, Committee on Graduate Students
Department of Electrical Engineering and Computer Science

Electrostatic Pull-in Test Structure Design for *in-situ* Mechanical Property Measurements of Microelectromechanical Systems (MEMS)

submitted to the Department of Electrical Engineering and Computer Science
in partial fulfillment of the requirements for the degree of Doctor of Philosophy

Raj K. Gupta

Abstract

M-TEST, an electrostatic pull-in approach for the *in-situ* mechanical property measurements of microelectromechanical systems (MEMS), is used to extract the Young's modulus and residual stress in polysilicon surface micromachined devices. Its high sensitivity to geometry is also used for process monitoring of device thickness and gap values. Cantilevers and fixed-fixed beams are designed, simulated, and tested for use with M-TEST.

M-TEST models for estimating pull-in voltages are developed from two-dimensional finite-difference and energy-method electromechanical calculations and three-dimensional finite-element mechanical simulations. They include transition of Young's modulus to plate modulus in thin and wide beams, stress-stiffening in fixed-fixed beams, compliant supports, and curling in cantilevers due to stress-gradients.

An optical microscope and standard electronic test equipment are used to observe and measure the pull-in voltages. Dektak surface-profilometry, capacitance measurements, and a calibrated translation stage are used to measure structural thickness, gap and length, and an optical tip deflection measurement is used to estimate cantilever curvature.

Combining knowledge of geometry with the bending and stress process parameters extracted from M-TEST allows mechanical property extraction. M-TEST is applied to 2 μm-thick polysilicon. Residual modeling errors are estimated to be 3%. The intrinsic precision in determining the average bending parameter from a set of 24 samples is 2%. At present, calibration uncertainties in measuring geometry limit the absolute accuracy of the extracted modulus to about 20%.

Thesis Supervisor: Stephen D. Senturia
Weller Professor of Electrical Engineering and Computer Science

Thesis Readers: Jeffery H. Lang
Professor of Electrical Engineering and Computer Science

Carl V. Thompson
Professor of Material Science and Engineering

Acknowledgments

Many individuals, friends and colleagues, have been instrumental in making this educational process a success. Pivotal in this role, was my research advisor Stephen Senturia, who taught me to "break through walls instead of jump over them", and gave me the opportunity to develop the fundamentals of doing scientific research in a setting where I was free to explore what interested me.

David Koester (MCNC) and Charles Hsu provided the samples tested in this work; X-ray measurements were done in the Material Science Department by Steve Seel; and MEMCAD expertise was provided by John Gilbert (Microcosm).

I have had the pleasure to share MIT Rm. 39-667 with friends - Fred Trusell (Ford Microelectronics), Daniel Sobek (AMD), Mathew Varghese and Erik Deutsch. We had some great laughs together, and occasionally found ourselves eating ice cream at Tosci's, enjoying a good BBQ, or even spending a day at the beach. Erik deserves a special thanks. He conducted some of the M-TEST measurements reported in this thesis at a crucial juncture in my thesis preparation.

Peter Osterberg (University of Portland) was invaluable for getting me off the ground after I first joined the group. The time he took to answer many of my innocent questions about research and the discussions that followed were a tremendous help. Thanks to Vladimir Rabinovich for having the patience to work out my UNIX-related blues and for helping me with MEMCAD, and to Scotti Fuller for recognizing my times in need, and for making them pass with grace.

My parents, Kailash and Ahilya Gupta, and my brother Ram have never doubted my ability or my desire to succeed. I am happy to be here today, and I am glad that I can share that happiness with them.

Table of Contents

Chapter 1: Introduction 1

1.1 Thesis Outline 2
1.2 Previous Work on Mechanical Property Extraction 2
1.3 The M-TEST Approach 3

Chapter 2: Theory and Simulations 5

2.1 The One-dimensional Model 5
2.2 M-TEST Models for Ideal Two-dimensional Geometries . . . 7
2.2.1 The Two-Dimensional Model 7
2.2.2 Numerical Finite-Difference Method 10
2.2.3 Rayleigh-Ritz Energy Method 10
2.3 M-TEST Models for Three-Dimensional Geometries 11
2.3.1 Plate Effects 12
2.3.2 Membrane Stiffness 16
2.3.3 Support Compliance 18
2.3.4 Stress-Gradients Through Film Thickness 21
2.3.5 Revised M-TEST Models 22

Chapter 3: Guidelines for Using M-TEST 23

3.1 Equipment Requirements for M-TEST 23
3.1.1 Pull-in Voltage Measurements 23
3.1.2 Metrology Measurements 25
3.2 Designing M-TEST Structures 26
3.2.1 Selecting Layout Dimensions in Limiting Cases 26
3.2.2 Selecting Layout Dimensions for the General Case 27

3.3 Mechanical Property Extraction using M-TEST 28
3.4 Estimating Error Bounds on Extracted Properties 28
3.4.1 Reducing Systematic Errors 29
3.4.2 Equations from Statistics Theory 29
3.4.3 Error Analysis for Revised M-TEST Models in the Limiting Cases . . 30
3.4.4 Error Analysis for Revised M-TEST Models in the General Case . . . 31
3.4.5 A Numerical Error Sensitivity Example 32

Chapter 4: Experimental Results 35

4.1 M-TEST Assessment of MEMS Process Integrity 35
4.1.1 Process Description 35
4.1.2 Measurements of Pull-in Voltage and Geometry 36
4.1.3 Analysis of Results 38
4.1.4 Accurate Modeling in Two- and Three-Dimensions 40
4.2 M-TEST Mechanical Property Extraction from Polysilicon . 41
4.2.1 Test Structure Fabrication 42
4.2.2 Pull-in Voltage Measurements 43
4.3 M-TEST Monitoring of Inter-Run and Intra-Run Variations . 46
4.3.1 Data from Cantilevers and Fixed-fixed Beams 46
4.3.2 A Comparison of the Results 47

Chapter 5: Discussion and Conclusions 51

5.1 Future Work and Applications 54
5.2 Conclusions 54

References 57

Appendix A: Silicon Mechanical Properties 63

Appendix B: Microscope Stage Design 67

CHAPTER 1

Introduction

With the commercialization of microelectromechanical systems (MEMS) for mechanical sensors, such as pressure sensors [1-5], accelerometers [6-8], gyroscopes [9-10], shear-stress sensors [11-13], and thermomechanical infrared sensors [14], and for mechanical actuators, such as projection displays [15-16], relays [17-18], and high-quality filters [19], there is an increasing need for an automatable method to routinely assess the uniformity and repeatability of a MEMS manufacturing process, and to extract critical performance parameters, such as process-sensitive thin film geometries and mechanical properties, for successful design and modeling of sensors and actuators [20]. One such method, which relies on wafer-level probing of electrostatic pull-in test structures, is called M-TEST [21-24]. This approach allows easy measurement, uses simply designed test structures that can be microfabricated *in-situ* alongside other sensors or actuators, and is tractable to well-developed models.

This thesis develops M-TEST for a recently commercialized MEMS foundry based on polysilicon surface-micromachining [25-27]. In previous work, prototype M-TEST models were successfully applied to well characterized low-stress single-crystal silicon microstructures with idealized geometries made by wafer-bonding [22-23, 28]. The extension of the M-TEST models to polysilicon surface micromachining presents a significant challenge because of large processing variations in thin film properties, stress-dependent structural geometries and complex three-dimensional electromechanical behavior [21].

1.1 Thesis Outline

The goals of this work are discussed by way of the thesis outline. This chapter along with providing the motivation and the reason for choosing M-TEST, discusses alternate methods for MEMS mechanical property extraction, and outlines the M-TEST strategy.

Chapter 2 begins with a simple explanation of electrostatic pull-in and a review of the ideal two-dimensional M-TEST models. Higher-order M-TEST models are developed for complex test structure geometry. Guidelines for implementing M-TEST are discussed in Chapter 3, and include practical design rules for test structures, equipment requirements, and an error sensitivity analysis for measured data. In Chapter 4, experimental results highlight the use of M-TEST to assess process integrity, to extract polysilicon mechanical properties, and to monitor inter-run and intra-run process and mechanical property variations in polysilicon surface micromachining. Chapter 5 compares the M-TEST extracted polysilicon mechanical properties to expected values and to those determined by other researchers. It concludes with suggestions for future work and a thesis summary.

1.2 Previous Work on Mechanical Property Extraction

Methods for *in-situ* characterization of the Young's modulus or the residual stress from microelectromechanical systems (MEMS) have involved the measurement of resonant frequencies from beams [29-35] and comb-drives [36-39], the observation of stress relaxation in buckling or rotating structures [40-42], the capacitance-voltage measurement of a fixed-fixed beam bridge [43], the displacement measurement of a cantilever tip with the application of a known mechanical force [44], and the measurement of electrostatic pull-in test structures [21-24, 29, 31, 40, 45]. *Ex-situ* techniques, which test specially designed large area devices, include the measurement of membrane deflection due to an applied pressure [46], and the measurement of tensile strain in centimeter-long hourglass structures axially-loaded by a piezoelectric translator [47].

A recent survey by Schweitz showed that there is general disagreement, by up to ±30% around *known* mechanical property values, using some of these methods [44]. Although, *ex-situ* techniques have shown better repeatability than *in-situ* techniques, the lack of either precise modeling, accurate representations of geometry, sound error reduction techniques, or adequate assumptions have made these measurement techniques prone to error.

Moreover, because *ex-situ* techniques do not allow integration with other sensors, they are of limited use for routine manufacturing quality control.

M-TEST, an *in-situ* technique based on electrostatic pull-in of beams (cantilevers and fixed-fixed beams) and diaphragms, allows integration and wafer-level probing using standard electronic test equipment. A fit of the measured pull-in voltages to analytical models based on two- and three-dimensional coupled electromechanical models and accurate measurements of geometry, enables simultaneous extraction of Young's modulus, residual stress and Poisson's ratio. M-TEST has demonstrated that the orientational-dependent Young's modulus in crystalline silicon can be measured to within 3% of known literature values [48].

Confidence in M-TEST suggests that it will work with other materials where the mechanical properties are initially unknown. Previously developed analytical models for ideal geometries developed by Osterberg in [22-24] are inappropriate for stress-dependent structures such as surface-micromachined MEMS devices, and hence, the M-TEST approach requires revised models which work in highly compressive, tensile or thickness-varying stress conditions, and with structures having compliant built-up supports. These issues and others will be addressed in this thesis. An M-TEST methodology will be developed, from these revised models and from the practical approach to device measurement, to extend M-TEST as a generally applicable tool for *in-situ* mechanical property extraction.

1.3 The M-TEST Approach

Figure 1.1 outlines the M-TEST approach. By itself, the pull-in voltage from a simple beam acts as a monitor for quality control. When multiple fixed-fixed beam lengths or diaphragm radii are tested and modeled, their pull-in voltage sensitivity to modulus and stress emerge separately, as the bending- and stress- parameters, B and S, respectively. B and S, which are a product of a mechanical property (stress or modulus) and high powers of geometry, enable a simple assessment of process uniformity across chip-to-chip, wafer-to-wafer and run-to-run. Specific examples are shown from the MIT silicon wafer-bonded MEMS process and a polysilicon surface-micromachined MEMS process.

Combining carefully measured thickness and gap geometry with B and S, the biaxial residual stress σ_o and the plate modulus $E/(1-\nu^2)$ can be extracted from diaphragms, the axial residual stress $\sigma_o(1-\nu)$ and Young's modulus E, from fixed-fixed beams, and E, from

cantilevers. The measurement of all three test structures enables, through simple algebra, independent extraction of E, σ_o, and ν. In this thesis, only fixed-fixed beams and cantilevers are tested, and, hence, only $\sigma_o(1\text{-}\nu)$ and E are obtained. Furthermore, since ν is typically 0.23 for polysilicon with random grain orientation [47, Appendix A], the biaxial residual stress can still be approximated from the axial residual stress.

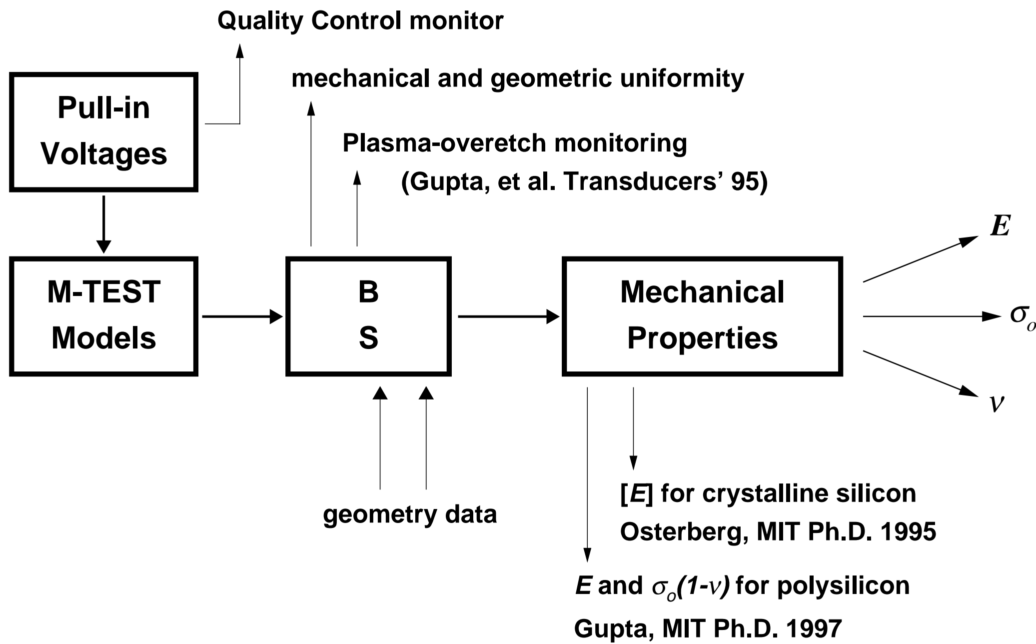

Figure 1.1: Outline of the M-TEST approach. Pull-in results from beams and circular diaphragms enable M-TEST to be used for quality control, and for extracting the Young's modulus E, the biaxial residual stress σ_o and the Poisson's ratio ν. In this thesis, polysilicon surface-micromachined beams will be used to extract E and $\sigma_o(1\text{-}\nu)$.

CHAPTER 2

Theory and Simulations

In this chapter, previously developed analytical M-TEST pull-in models based on two-dimensional simulation will be revised to reflect three-dimensional mechanical effects found in thin nonplanar MEMS geometries fabricated by a conformal deposition processes, like polysilicon surface-micromachining.

This chapter begins with a short description of electrostatic pull-in for a lumped one-dimensional model. It follows with a review of the ideal two-dimensional M-TEST electromechanical model used to calculate the static pull-in voltage. Analytical models fit to these calculations for automated mechanical property extraction have been presented in previous research, and are repeated here for reference. Later chapter sections quantify perturbations of the ideal two-dimensional models for three-dimensional geometries to include: (1) transition from Young's modulus to plate modulus for wide beams, (2) nonlinear geometric deformation, (3) compliance of built-up supports, and (4) curling of cantilever beams due to stress-gradients through the film thickness.

Two-dimensional finite-difference equations and energy methods, and three-dimensional mechanical simulations are used to investigate the four cases above, and their results are incorporated into revised analytical M-TEST models.

2.1 The One-dimensional Model

The one-dimensional model is shown in Figure 2.1. It is electrostatically actuated by an applied DC voltage across rigid parallel plates, where one plate is fixed and the other is

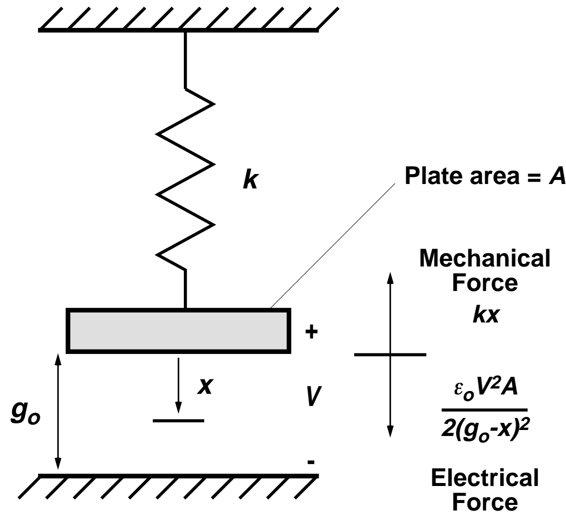

Figure 2.1: Schematic of one-dimensional electrostatic pull-in model. The parallel plates are held apart by a spring force, and the electrostatic force pulls them together.

attached to a spring. The displacement versus voltage characteristic for this geometry is shown in Figure 2.2. The coupled electromechanical system becomes unstable at the static pull-in voltage $V_{PI} = (8kg_o^3/27\varepsilon_o A)^{1/2}$, a point a which the movable plate is displaced one-third of the original gap g_o. In this equation, k is the spring constant, and ε_o is the permittivity of air. Note, this simple expression shows that V_{PI} scales with the square root of stiffness and a 3/2 power of the original gap.

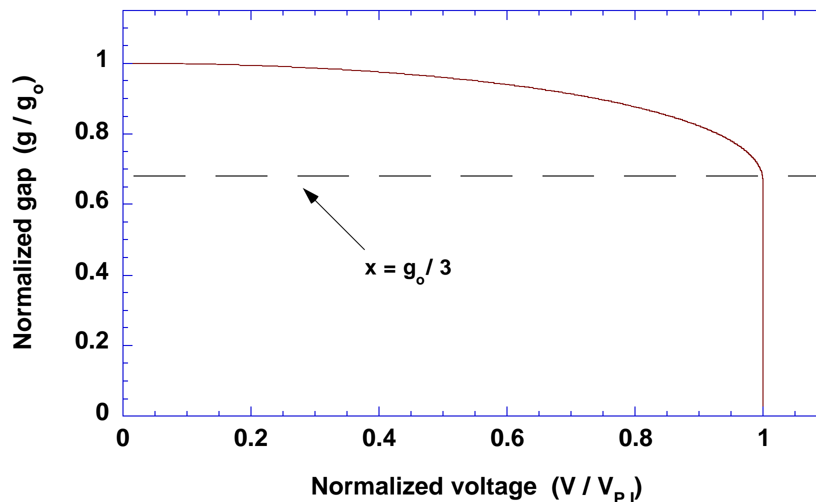

Figure 2.2: Gap versus voltage for the one-dimensional model, showing the pull-in instability at a displacement of one-third the original gap.

2.2 M-TEST Models for Ideal Two-dimensional Geometries

A schematic of the three types of M-TEST structures are shown in Figure 2.3. They are the cantilever beam (n = 1), the fixed-fixed beam (n = 2) and the clamped circular diaphragm (n = 3), where n is an index for structure type which is frequently used in the subscripts of the bending- and stress-parameter B_n and S_n. These structures are electrostatically actuated over an initial ideally uniform gap of g_o to a position dependent gap g, by an increasing DC bias voltage between the fixed-ground conductor and the conducting movable structure supported by ideally fixed ends. A two-dimensional model is used to calculate the mechanics of the test structures and includes the effects of in-plane biaxial residual stress. The static pull-in voltage is determined by coupling the mechanics to a nonlinear voltage-dependent electrostatic pressure term and finding the lowest voltage at which the system is unstable.

2.2.1 The Two-Dimensional Model

The two-dimensional Bernoulli-Euler beam bending theory is used to model the test structure mechanics. The theory assumes: (1) small deflections for which the radius of curvature equals the inverse of the second-derivative of deflection, (2) no shear deformation from transverse loading, and (3) no in-plane (longitudinal, width-wise, or radial) curvature

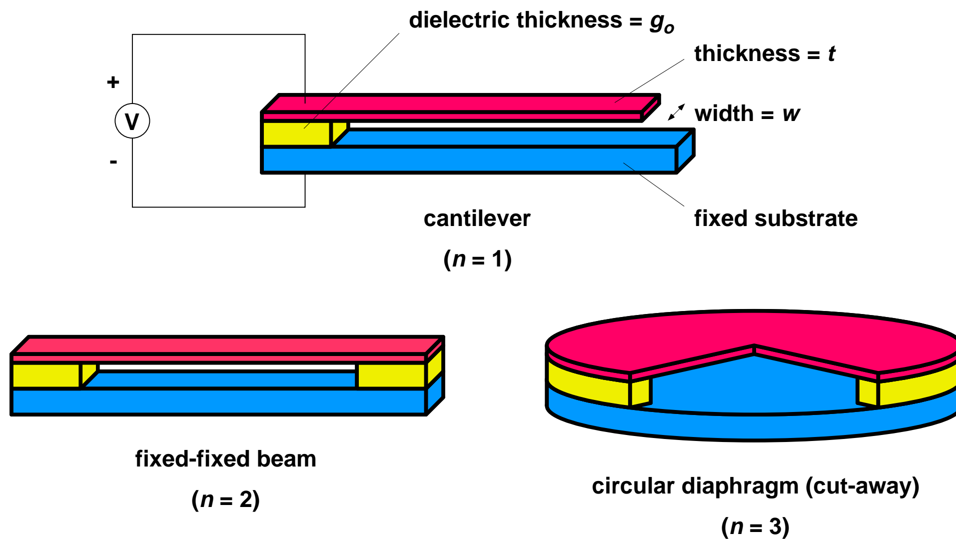

Figure 2.3: Ideal M-TEST structures having planar geometry, nearly fixed ends, uniform gap and dielectric isolation. Electrostatic voltage is applied between the conducting beam or diaphragm and substrate.

adjustments due to transverse (vertical) extension or compression of the thickness from a transverse (vertical) load. These assumptions are valid for typical vertically-actuated MEMS geometries which have large in-plane dimensions compared to their thicknesses and gaps. To model the ideal M-TEST structures, we additionally assume that: (4) the supports are ideally fixed, (5) the gap is uniformly g_o in the unloaded state, (6) membrane effects from stress-stiffening are negligible, and (7) anticlastic curvature along a beam's width w is geometrically insignificant, but the plate-like changes in stiffness as w increases can be modeled by adjusting the effective modulus $\tilde{E}$.

The coupled electromechanical equation is shown in general form for the three test structure types in equation (2.1). The electrostatic pressure (right-hand side) is derived from a parallel-plate approximation with an applied voltage V, and has a fringing-field correction f_f equal to $0.65\ g/w$ for beams with a small gap to width ratio [50-51].

$$\tilde{E}\hat{I}\nabla^4 g - \hat{T}\nabla^2 g = -\frac{\varepsilon_o V^2}{2g^2}\left(1+f_f\right) \tag{2.1}$$

For beams which are narrow relative to their thickness and length, $\tilde{E}$ is the Young's modulus E. For beams, which are wide relative to their thickness and length, and for circular diaphragms, $\tilde{E}$ is the plate modulus $E/(1-\nu^2)$, where ν is Poisson's ratio [52]. $\widehat{I}$ equals $t^3/12$, where t is the film thickness. $\widehat{T}$ equals $\tilde{\sigma}t$, where the thickness-averaged $\tilde{\sigma}$ is positive in tension. $\tilde{\sigma}$ equals the biaxial residual stress σ_o for circular diaphragms, and the uniaxial residual stress $\sigma_o(1-\nu)$ after the Poisson relaxation for fixed-fixed beams. For cantilevers, which are stress-free, $\widehat{T}$ equals zero. In general, the product $\tilde{E}\widehat{I}$ is calculated by an integral. This is necessary for multilayered structures [53].

Because of lateral symmetry in beams and radial symmetry in circular diaphragms, equation (2.1) is two-dimensional - in length L or radius R, and in gap g. This is shown in detail in equation (2.2) for beams, where the x-axis is parallel to the beam length, and in equation (2.3) for circular diaphragms, where the r-axis is in polar coordinates and radiates from the center of the diaphragm.

$$\tilde{E}\hat{I}\frac{d^4 g}{dx^4} - \hat{T}\frac{d^2 g}{dx^2} = -\frac{\varepsilon_o V^2}{2g^2}\left(1+f_f\right) \tag{2.2}$$

$$\tilde{E}\hat{I}\left\{\frac{d^4 g}{dr^4} + \frac{2}{r}\frac{d^3 g}{dr^3} - \frac{1}{r^2}\frac{d^2 g}{dr^2} + \frac{1}{r^3}\frac{dg}{dr}\right\} - \hat{T}\left\{\frac{d^2 g}{dr^2} + \frac{1}{r}\frac{dg}{dr}\right\} = -\frac{\varepsilon_o V^2}{2g^2} \tag{2.3}$$

By algebra, equation (2.1) can be written as equation (2.4), where, B and S are the bending- and stress-parameter, as defined in [23, 54], and equal $\tilde{E}t^3g_o^3$ and $\tilde{\sigma}tg_o^3$, respectively. The non-dimensionalized gap $\tilde{g}$, equals g/g_o. From this form, we observe that V_{PI} is primarily dependent on the variables B, S, and L or R, and that there is a small adjustment for fringing-fields in beams which is dependent on g_o/w.

$$\frac{1}{12}B\nabla^4\tilde{g} - S\nabla^2\tilde{g} = -\frac{\varepsilon_o V^2}{2\tilde{g}^3}\left(1+f_f\right) \tag{2.4}$$

$V_{PI,\ IDEAL}$		
General	**Bending-Dominated** ($SL^2/B \rightarrow 0$)	**Stress-Dominated** ($SL^2/B \rightarrow \infty$, $S > 0$)
$\sqrt{\dfrac{\gamma_1 S}{\varepsilon_o L^2 D(\gamma_2, k, L)\left[1+\gamma_3 \dfrac{g_o}{w}\right]}}$	$\sqrt{\dfrac{4\gamma_1 B}{\varepsilon_o L^4 \gamma_2^2\left(1+\gamma_3 \dfrac{g_o}{w}\right)}}$	$\sqrt{\dfrac{\gamma_1 S}{\varepsilon_o L^2\left(1+\gamma_3 \dfrac{g_o}{w}\right)}}$
where, $D = 1+\dfrac{2\{1-\cosh(\gamma_2 kL)\}}{\gamma_2 kL\sinh(\gamma_2 kL)}$, $k=\sqrt{\dfrac{3S}{B}}$, $S=\tilde{\sigma}tg_o^3$, $B=\tilde{E}t^3g_o^3$		

Table 2.1: Closed-form M-TEST models for ideal test structures [23]. (Note, $L = R$ for circular diaphragms.)

Numerical Constants	Cantilever (n = 1)	Fixed-fixed Beam (n = 2)		Circular Diaphragm (n = 3)
γ_1	**0.07**	**2.79**	**2.96***	**1.55**
γ_2	**1.00**	**0.97**	**1.00***	**1.64***
γ_3	**0.42**	**0.42**		**0**

Table 2.2: Numerical constants used in Table 2.1. Entries without asterisks are from [23]. Asterisk(*)-labelled constants are new and are based on revised M-TEST models for better accuracy in compressive stress conditions.

Numerical finite-difference MATLAB scripts [54-55] and Rayleigh-Ritz energy methods [31] have been used for evaluating the pull-in voltage from equation (2.4). For the ideal test structure (geometrically linear) the V_{PI}'s from the finite-difference scripts were reproduced accurately using full three-dimensional MEMCAD simulations [54], and were approximated to analytical forms, as summarized in Table 2.1-2.2. These analytical forms were originally derived for tensile or low stress cases, where SL^2/B is greater than zero. In the case of fixed-fixed beams and diaphragms, some constants, as indicated, are updated based on recent M-TEST model calculations for the compressive stress cases.

2.2.2 Numerical Finite-Difference Method

The finite-difference scripts solve for V_{PI} in either of two ways. Both increment the applied voltage until pull-in occurs and rely on a discretized nodal array. However, at a given voltage, the first approach (the relaxation method) iterates between separate calculations of the deformation and of the electrostatic pressure until they are mutually consistent. The second approach (Newton's method) starts from a given deflection and assumes that the actual deflection is a small δ away. Expansion of the differential equation by Taylor series about the given deflection separates the δ from the known constants. The δ is solved by matrix operation. The δ is added to the initial deflection, and the procedure is iterated with the new deflection until δ converges within a specified tolerance.

2.2.3 Rayleigh-Ritz Energy Method

The Rayleigh-Ritz energy method uses a deflection approximation *m(x)*, obeying suitable boundary conditions, to estimate an upper bound for V_{PI} and to calculate the generalized coordinate (deflection amplitude) A at this voltage. An an upper bound close to V_{PI} relies on a good guess for *m(x)*. The system's total potential energy U_{TOT} due to electrostatic deflection is evaluated at an applied voltage V and an amplitude-scaled version of m. U_{TOT} is shown below in equation (2.5) for the beam example of equation (2.2), where f_f is set to zero for simplicity.

$$U_{TOT} = \frac{w}{2}\int_0^L \left\{ \tilde{E}\hat{I}\left(\frac{\partial^2 (Am)}{\partial x^2}\right)^2 + \hat{T}\left(\frac{\partial (Am)}{\partial x}\right)^2 - \frac{\varepsilon_o V^2}{g_o - Am} \right\} dx \qquad (2.5)$$

The equilibrium solution ($\partial U_{TOT}/\partial A = 0$) becomes unstable ($\partial^2 U_{TOT}/\partial A^2 = 0$) at the pull-in voltage. Based on these two conditions, the maximum value of A and $V = V_{PI}$ are obtained simultaneously.

Using $m(x)$ equal to $g_o \times [1-cos(2\pi x/L)]$ for fixed-fixed beams, an analytic solution for A and V_{PI} can be obtained. The results are summarized below in equations (2.6).

$$U_{TOT} = \frac{\pi^2 w}{3 g_o L^3}\left(\pi^2 B_2 + 3 S_2 L^2\right) A^2 - \frac{\varepsilon_o w V^2 L}{2 g_o \sqrt{1-2A}}$$

$$V_{PI} = \frac{\pi^2}{L^2}\sqrt{\frac{4\sqrt{3/5}}{25}\frac{B_2}{\varepsilon_o}\left(1+\frac{3 S_2 L^2}{\pi^2 B_2}\right)} \qquad \text{and} \qquad A = \frac{1}{5} \tag{2.6}$$

Because this deflection shape is the first Euler-buckling mode for fixed-fixed beams and closely resembles the electrostatic deflection profile, as determined by two-dimensional finite-difference simulations, for highly compressive, but unbuckled fixed-fixed beams, excellent agreement is found between pull-in voltages from the numerical calculations and the energy-method in this regime. In contrast, in the high-tensioned stress-dominated regime, where the bending-energy term is negligible, a parabolic-like deflection shape for the fixed-fixed beam, gives more accurate results.

2.3 M-TEST Models for Three-Dimensional Geometries

General applicability of M-TEST requires that models accurately handle complex three-dimensional or nonlinear mechanics wherever the analytical models developed for ideal test structures become inaccurate. This is the case for thin structures with built-up supports

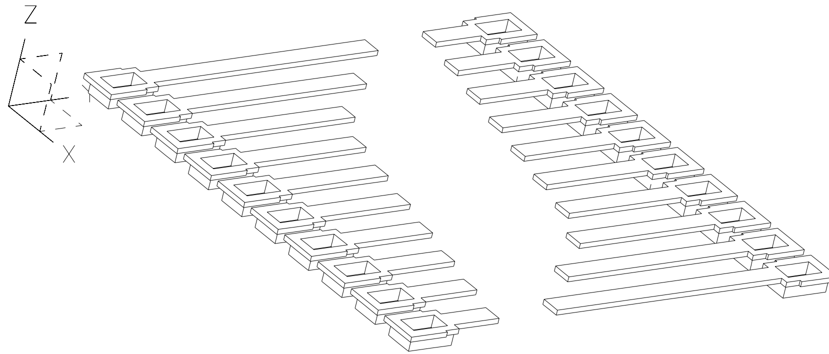

Figure 2.4: MEMBUILDER-created geometry in I-DEAS of 40 μm wide surface micromachined cantilevers of varying lengths from 100 μm to 500 μm. Vertical dimensions, of the 2 μm gap, the 2 μm thickness and the built-up supports, are exaggerated for clarity.

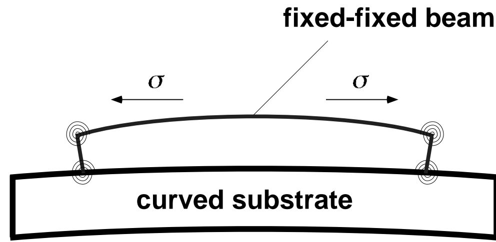

Figure 2.5: A simplified schematic of a fixed-fixed beam on (spring-like) torsionally-compliant built-up supports shows the deformation of the beam due to compressive residual stress and a deformed substrate.

and stress-dependent geometry made, for example, by the conformal polysilicon deposition process of surface-micromachining. (See Figure 2.4) Wide beams, which are short and thin and have fixed ends, exhibit plate-like behavior from transverse loading which increase their stiffness. Thin structures supported at opposite ends exhibit membrane stiffness when deformed more than their thickness [52]. Furthermore, built-up supports increase structural compliance [26, 56-58], and rotate in the presence of residual stress compromising the constant gap assumption for ideal structures under zero electrostatic load. (See Figure 2.5) Cantilevers will curl out of plane due to residual stress-gradients in the film thickness [59]. (See Figure 2.6) In combination, these effects can cause significant shifts in the pull-in voltage, and hence, if not modeled or understood properly, they will undermine the accuracy of extracted mechanical properties using M-TEST.

In this section, many of the effects mentioned above will be simulated using a combination of two- and three-dimensional models. Analytical M-TEST models will be revised based on the simulation results.

2.3.1 Plate Effects

Plate effects, which increase beam stiffness and arise in beams with fixed ends that are wide relative to their thickness and length, are modeled using I-DEAS FEM. An array of varying length and width cantilevers and fixed-fixed beams of unit thickness, are loaded by

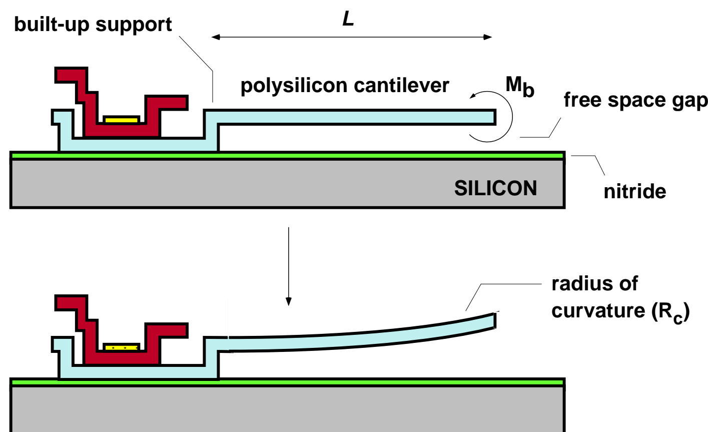

Figure 2.6: Cross-section of a polysilicon cantilever with a built-up support anchored on a nitride layer, dielectrically isolating it from the silicon substrate. The stress gradient is modeled as a bending moment M_b applied to the initially flat cantilever causing a curling radius R_c.

a uniform transverse (vertical) pressure to simulate electrostatic pressure loading. The pressure is equally divided between the top and bottom surfaces of the beam to avoid thickness extension, and, hence, small changes in in-plane curvatures, due to electrostatic loading which appears only on the bottom surface. The deformation is solved using linear statics. By symmetry, only a half of the cantilever and a quarter of the fixed-fixed beam are meshed. A $60 \times 15 \times 5$ parabolic-brick mesh is used along the length, width and thickness, respectively. The Young's modulus E and Poisson's ratio ν are chosen to be 162 GPa and 0.23, respectively, based on the crystalline average of silicon, to represent polysilicon with random grain orientation ([60, 61], Appendix A).

The width-averaged tip deflection $\tilde{\delta}_{tip}$ of a cantilever and center deflection $\tilde{\delta}_{center}$ of a fixed-fixed beam are taken from the deformed FEM mesh, and then normalized by division to the analytical results, δ_{tip} and δ_{center}, from the narrow beam limit where the plate effect is negligible. Under a uniform pressure load of q, the analytical results are given by equations (2.7) and (2.8), for the cantilever and fixed-fixed beam, respectively.

$$\delta_{tip} = \frac{3qL^4}{2Et^3} \tag{2.7}$$

$$\delta_{center} = \frac{qL^4}{32Et^3} \tag{2.8}$$

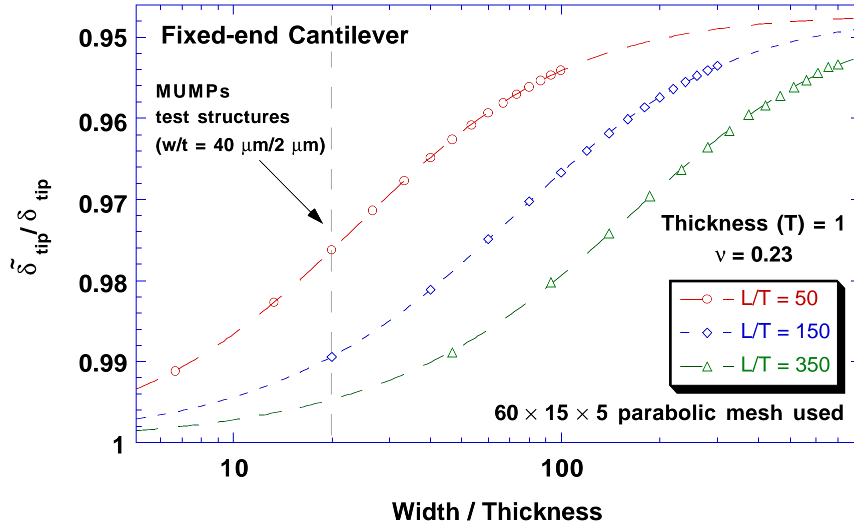

Figure 2.7: FEM simulation (data points) of width-averaged cantilever tip deflections $\tilde{\delta}_{tip}$ normalized to the analytical solution δ_{tip} for varying beam geometry. Dashed lines are curve fits to equation (2.11). Note, the ratio approaches $(1\text{-}\nu^2)$, which equals 0.947 for $\nu = 0.23$.

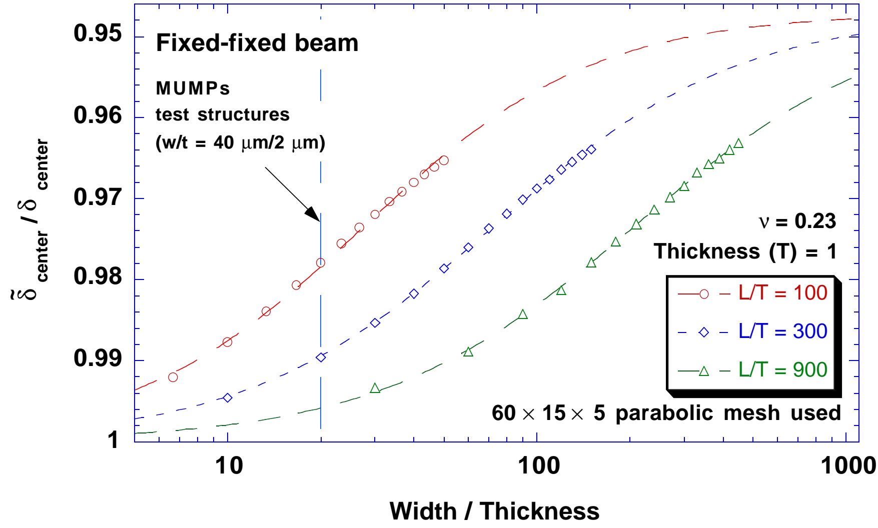

Figure 2.8: FEM simulation (data points) of width-averaged fixed-fixed beam center deflections $\tilde{\delta}_{center}$ normalized to the analytical solution δ_{center} for varying beam geometry. Dashed lines are curve fits to equation (2.12). Note, the ratio approaches $(1\text{-}\nu^2)$, which equals 0.947 for $\nu = 0.23$.

The graphs from the normalized calculations are shown in Figures 2.7-2.8. As expected, for wider and thinner beams the ratio approaches the Young's modulus divided by the plate modulus, which is $(1\text{-}\nu^2)$ and equals 0.947 for $\nu = 0.23$, and is independent of E.

To model the effects of arbitrary ν, a two-dimensional beam is conceptually divided into two regions of differing stiffnesses. As shown in Figure 2.9, the first region extends a length of L_{plate} from each fixed end, and its bending is determined by the plate modulus. The second region constitutes the remaining beam length, and its bending is determined by the Young's modulus. The ratio L_{plate}/L determines the relative influence of the plate-like behavior and generally increases with w, or with a reduction in L or in t. Using two-dimensional Bernoulli-Euler mechanics, analytical solutions for the cantilever tip deflection $\tilde{\delta}_{tip}$ and for the fixed-fixed beam center deflection $\tilde{\delta}_{center}$ are obtained as a function of L_{plate}/L. They are shown in equations (2.9) and (2.10).

$$\tilde{\delta}_{tip} = \frac{3qL^4}{2Et^3}\left\{1 - \upsilon^2\left[\frac{4}{3}\left(\frac{L_{plate}}{L}\right)^3 - \frac{1}{3}\left(\frac{L_{plate}}{L}\right)^4\right]\right\} \tag{2.9}$$

$$\tilde{\delta}_{center} = \frac{qL^4}{32Et^3}\left\{1 - \upsilon^2\left[2\left(\frac{2L_{plate}}{L}\right)^3 - \left(\frac{2L_{plate}}{L}\right)^4\right]\right\} \tag{2.10}$$

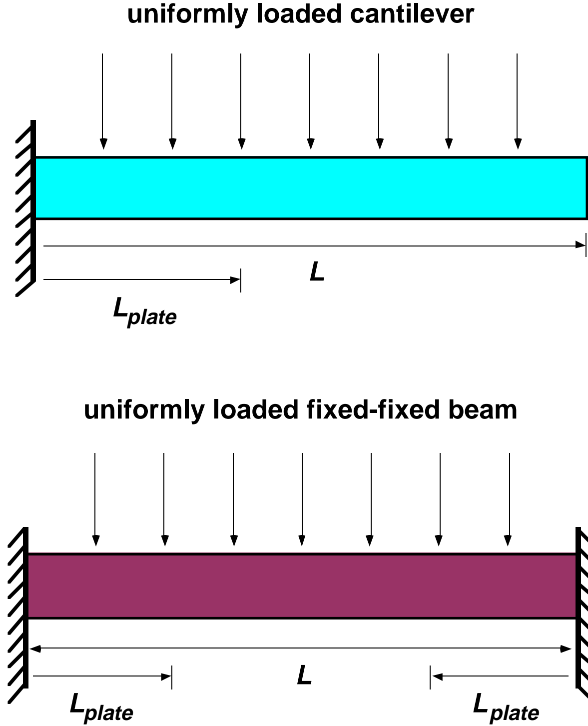

Figure 2.9: The L_{plate}-model used for calculating effective moduli for various beam geometries and arbitrary ν.

Equations (2.9) and (2.10) separate the influence of ν from L_{plate}. This enables analytical fits of the bracketed terms, containing only constants and L_{plate}/L, to FEM simulations for $\tilde{\delta}_{tip}$ and $\tilde{\delta}_{center}$ as a function of L, w, and t, for arbitrary ν. These simulations use $\nu = 0.23$ and $E = 162$ GPa, as a point of reference. Based on the fits shown in equations (2.11) and (2.12), the effective modulus $\tilde{E}$ can be expressed as a product of E and the ratio $\delta/\tilde{\delta}$.

$$\frac{E}{\tilde{E}} = \frac{\tilde{\delta}_{tip}}{\delta_{tip}} \approx 1 - \upsilon^2 \left[\frac{(w/L)^{1.37}}{0.5 + (w/L)^{1.37}} \right]^{0.98 \left({}^{L}\!/\!{}_{t} \right)^{-0.056}} \tag{2.11}$$

$$\frac{E}{\tilde{E}} = \frac{\tilde{\delta}_{center}}{\delta_{center}} \approx 1 - \upsilon^2 \left[\frac{(w/L)}{0.18 + (w/L)} \right]^{1.77 \left({}^{L}\!/\!{}_{t} \right)^{-0.061}} \tag{2.12}$$

The above values of $\tilde{E}$, which have the proper adjustment for plate effects, is used in the ideal M-TEST models of Table 2.1. These results indicate that $\tilde{E}$ is primarily dependent on w/L and weakly dependent on L/t, as seen in the graphs of $\tilde{\delta}_{tip}$ and $\tilde{\delta}_{center}$ in Figure 2.10.

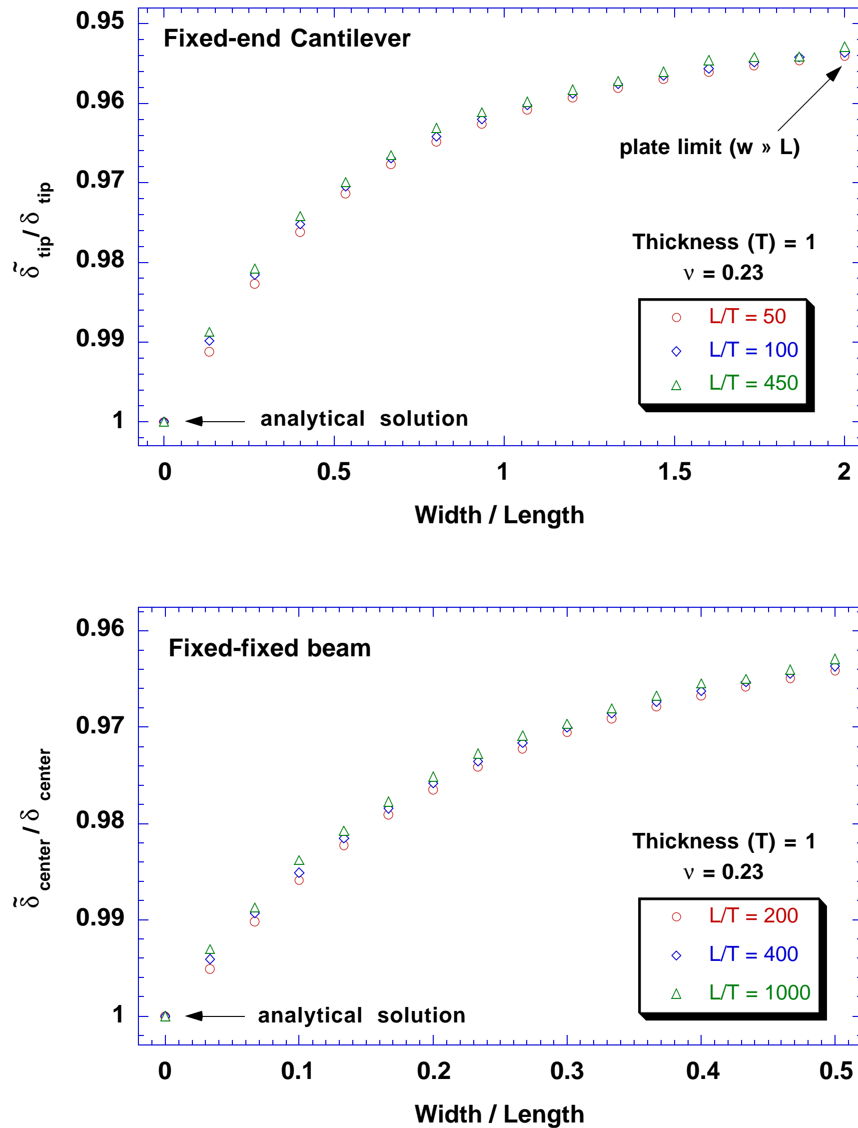

Figure 2.10: The two graphs show that FEM data points for normalized average cantilever tip deflection $\tilde{\delta}_{tip}/\delta_{tip}$ and fixed-fixed beam center deflection $\tilde{\delta}_{center}/\delta_{center}$ have a strong sensitivity to *w/L*, and weak dependence on *L/t*.

Note, because $\tilde{E}$ is derived for uniform pressure loading, it will not be accurate in place of E for other types of loading situations found, for example, in point loading of beams or in microbeam resonance.

2.3.2 Membrane Stiffness

Membrane effects due to stress-stiffening are present in structures having non-translatable supports on opposite sides. This increases structural stiffness significantly when the

maximum deflection is on the order of the thickness in the direction of the deflection, due to an increasing nonlinear $\widehat{T}$ term which is a function of structural deformation.

An energy-based approach which can used to determine the effect of membrane stiffness on V_{PI} is useful in developing intuition, but is not as accurate as finite-difference simulations. Nevertheless, to see how such an approach can be developed is instructive. Its results also help to formulate analytical curve fit solutions for the finite-difference simulations.

An added potential energy term is required for the increased in-plane tension as the structure deforms. For an ideal fixed-fixed beam with a membrane term, the potential energy added to the U_{TOT} from equation (2.5), is shown in equation (2.13) [62].

$$U_{TOT,\,NL} = U_{TOT} + \frac{w}{2}\int_0^L \left\{ \frac{\tilde{E}t}{4}\left(\frac{\partial(Am)}{\partial x}\right)^4 \right\} dx \tag{2.13}$$

If a sinusoidal deflection shape $m(x)$ equal to $g_o \times [1\text{-}cos(2\pi x/L)]$, obeying the fixed-boundary conditions at $x = 0$ and $x = L$, is used in combination with the definitions for B_2 and S_2, $U_{TOT,\,NL}$ can be fully integrated. $U_{TOT,\,NL}$ is shown as $\tilde{U}_{TOT,\,NL}$ in equation (2.14), after factoring out constants.

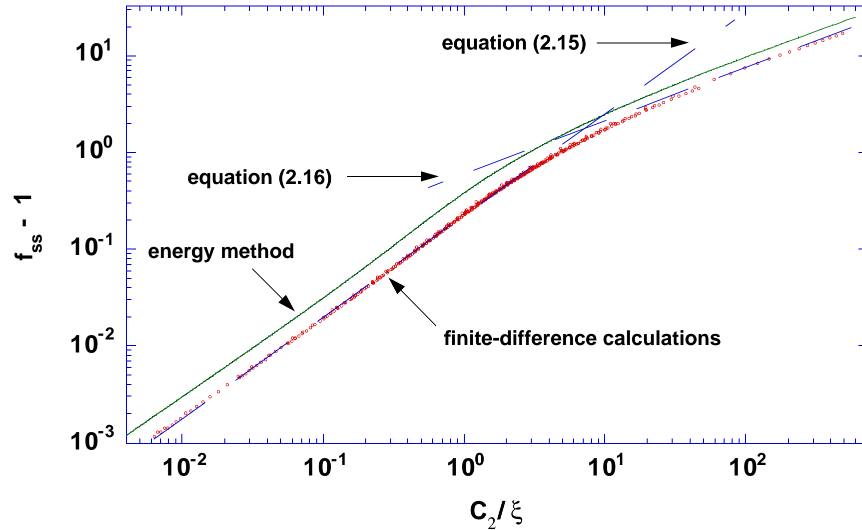

Figure 2.11: Stress-stiffening calculations for f_{ss}, the ratio of V_{PI}'s from the nonlinear-geometric case, which includes membrane effects, to the ideal linear-geometric case. The curve fits of equations (2.15) and (2.16) to the finite-difference calculations (small points) are shown as dashed lines.

$$\tilde{U}_{TOT,\,NL} = A^2 + \frac{9 C_2 A^4}{4\xi} - \frac{3 \varepsilon_o V^2 L^4}{2 \pi^4 B_2 \xi \sqrt{1-2A}}$$

$$\text{where,} \qquad \xi = 1 + \frac{3 S_2 L^2}{\pi^2 B_2} \tag{2.14}$$

In equation (2.14), C_2 equals $\alpha_2(g_o/t)^2$. The stress-relaxation factor α_2, from the support compliance, equals one for ideal fixed-fixed beams, and is discussed in the next section. C_2 enters only in the membrane stiffness term of equation (2.14), which, as expected, for small g_o/t can be neglected. Furthermore, when S_2L^2/B_2 approaches $-\pi^2/3$, the Euler buckling limit for fixed-fixed beams, membrane effects can significantly influence the mechanics. From scaling arguments, the ratio f_{ss} of the pull-in voltage from the stress-stiffened case to the pull-in voltage from the ideal case is found to be dependent solely on C_2/ξ.

Finite-difference simulations for calculating V_{PI} of stress-stiffened fixed-fixed beams are based on the relaxation method using a MATLAB script [55]. As the structure deflects, the increase in the membrane stress is modeled as a uniform increase in $\widehat{T}$ based on the beam's total elongation. Simulations are performed on a range of values for ξ and C_2, for both, the geometrically-nonlinear stress-stiffened case, and the ideal geometrically-linear case. Fringing-field effects are neglected for simplicity. The ratio f_{ss} is determined from these calculations and curve fit for $C_2/\xi < 3$, in equation (2.15), and for $C_2/\xi > 5$, in equation (2.16).

$$f_{ss} \approx 1 + 0.222\left(\frac{C_2}{\xi}\right)^{1.047} \tag{2.15}$$

$$f_{ss} \approx 1 + 0.499\left(\frac{C_2}{\xi}\right)^{0.579} \tag{2.16}$$

The finite-difference results are compared to energy-method calculations as shown in Figure 2.11. As expected, the energy-method over-estimates f_{ss}, but its general trend is very similar to the finite-difference results.

2.3.3 Support Compliance

Built-up supports found in conformal deposition processes of MEMS fabrication, as shown in Figure 2.4, increase not only structure compliance, but also rotate in the presence

of external moments from built-in residual stress, causing stress relief and changing the three-dimensional profiles of ideally uniform gap structures supported on opposite sides.

Modeling effects of support compliance require three-dimensional FEM simulation. The I-DEAS MEMBUILDER script [54, 63] is used to construct the three-dimensional support geometry from the two-dimensional masks used for actual device fabrication. The meshed geometry created in I-DEAS is passed for mechanical simulation into I-DEAS' own FEM solver or into ABAQUS.

I-DEAS FEM simulations are used to calculate tip deflections of uniformly pressure-loaded cantilevers for various mask-drawn lengths L_{mask} to determine bending compliance changes due to built-up supports. As an example, cantilevers fabricated by the MUMPs process are considered. They are given an E = 162 GPa, a ν = 0.23, a nominal thickness of 2 µm and a support height, obtained from the thickness of the sacrificial oxide layer, of 2 µm. The support thickness also has the same thickness as the beam in an ideal LPCVD process. Schematically, the beam geometries, as constructed from MEMBUILDER, are shown in Figure 2.4. The beams are simulated using parabolic tetrahedral elements with near unity aspect ratios and lateral dimensions equal to the beam thickness. Tip deflections from the simulations are plotted on a log-log scale and fit to the analytical form of equation (2.7) with a constant additive offset ΔL for length. As shown in Figure 2.12, a ΔL of 5.85 µm gives an excellent fit.

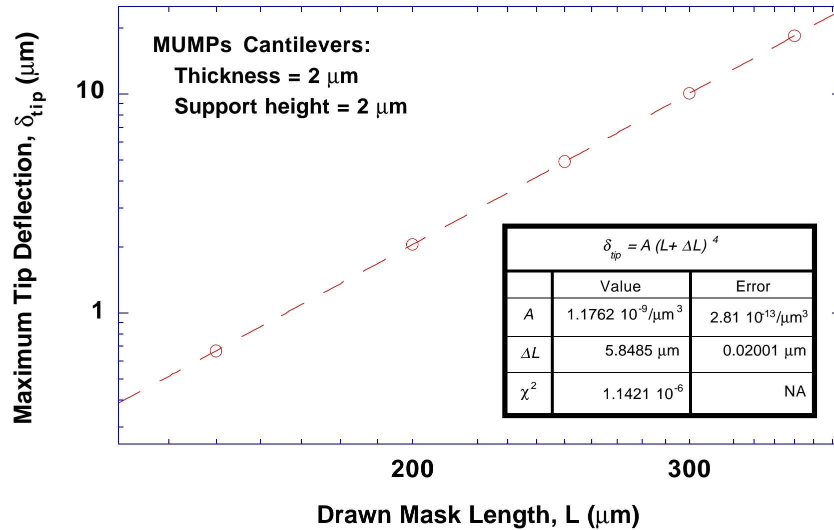

Figure 2.12: FEM simulations of uniformly loaded cantilevers with nominal thickness, gap and built-up support dimensions obtained from the MUMPs surface-micromachined polysilicon process, indicate that the built-up support compliance can be adjusted by a ΔL.

Simulations indicate, that in general when $\Delta L \ll L_{mask}$, support bending compliances can be modeled accurately by an offset in length. Similar conclusions can be drawn for fixed-fixed beams and circular diaphragms. Based on these FEM's, $L = L_{mask} + \Delta L$ is used in the ideal M-TEST models in Table 2.1.

Residual stresses in fixed-fixed beams and circular diaphragms cause support rotations from shear loading. This affects the equilibrium stress state, and can significantly alter structural geometry in the case of compressive stress. Fixed-fixed beams with built-up supports and an initial tensile biaxial residual stress σ_o, are meshed similarly to the cantilevers above, and solved in ABAQUS. After the beams deform from the initial stress load, the structures are individually assigned a stress-relaxation factor α_2, equal to $\tilde{\sigma}'/\tilde{\sigma}$, where $\tilde{\sigma}'$ is the final stress state and $\tilde{\sigma}$ equals $\sigma_o(1-\nu)$. For the MUMPs process, α_2 very nearly equals one for all of the fabricated lengths. However, when $g_o^3/(Lt^2)$ is larger than 0.1, α_2 can become smaller than 0.9. Furthermore, addition of another conformal step along the beam length away from the support, for example, due to a patterned underlying conductor as shown in Figure 2.13, can also affect α_2. After the correct geometry is modeled and α_2 is determined, $\tilde{\sigma}$ is redefined to equal $\alpha_2\sigma_o(1-\nu)$ for use in the ideal fixed-fixed beam M-TEST model of Table 2.1. A similar analysis, if necessary, can be made for the stress relaxation factor α_3 of clamped circular diaphragms. Note, based on linearly geometric elastics, α is no different for the compressive stress case than for the tensile case, unless the structure becomes highly deformed as explained below.

Support rotations cause pre-buckled bending in fixed-fixed beams and in circular diaphragms with high compressive residual stress below the buckling limit, as shown in Figure 2.5. Since this deformation can be large and its mechanics, geometrically nonlinear, the ideal M-TEST models designed for uniform gap will be invalid. Furthermore, due to the sensitivity of pre-buckled bending to boundary conditions and to stress-gradients, modeling this effect for the M-TEST models is inappropriate. Unfortunately, the design of ideal fixed ends is impossible, and therefore, M-TEST structures should be fabricated with lateral dimensions small enough such that pre-buckled bending is negligible.

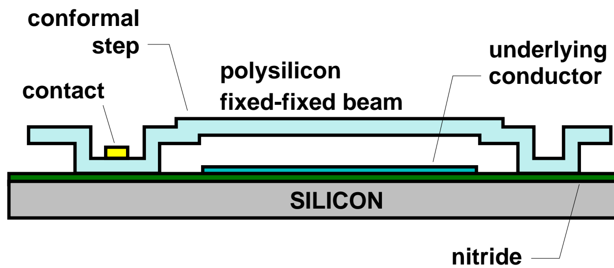

Figure 2.13: Polysilicon surface micromachined fixed-fixed beam with built-up supports and conformal steps along beam length due to an underlying conductor.

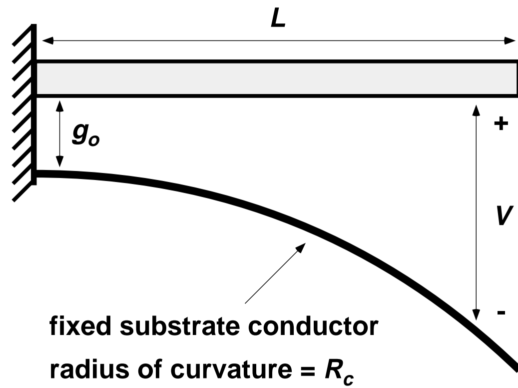

Figure 2.14: Cantilevers curled out-of-plane due to stress-gradients are modeled (in the limit of geometrically-linear elasticity) for 2D finite-difference calculations as being flat with a fixed curved substrate.

2.3.4 Stress-Gradients Through Film Thickness

Nonuniform stresses in the film thickness create built-in moments, which in released cantilevers cause them to curl out of plane, and in fixed-fixed beam with compliant supports and net compressive residual stress, to bow, as mentioned earlier. Because of the large possible deflections in gap from these structures, the electrostatic pressure is significantly modified from the corresponding uniformly flat case and the pull-in voltages can be significantly shifted.

M-TEST models for curled cantilevers are based on the two-dimensional Bernoulli-Euler beam theory, and neglect fringing fields and plate effects for simplicity. Models for the bowed fixed-fixed beams are not developed for the reasons mentioned in section 2.3.3.

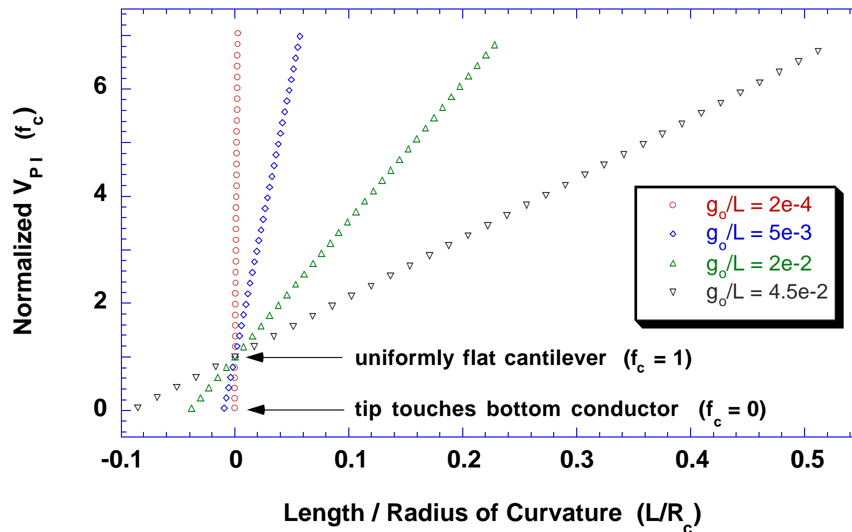

Figure 2.15: 2D finite-difference simulations of cantilever pull-in voltages calculated for various lengths L, gaps g_o and radii of curvature R_c, are divided by the pull-in voltage from the uniformly flat case ($R_c = \infty$) to get the normalized V_{PI}.

Because the stress-gradient is assumed to be uniform in-plane, the cantilever experiences a constant bending moment along its length when it is flat and has a constant radius of curvature R_c after it is released. Due to linearity for small deflections, the cantilever beam is modeled as initially flat with a curved fixed ground electrode, as shown in Figure 2.14. The pull-in voltages, from the curved geometry are calculated using finite-difference scripts, and then divided by the pull-in voltages from the ideal uniformly flat case. Selected results from the calculation of this ratio f_c are graphed in Figure 2.15. In terms of the non-dimensionalized term $L^2/(g_oR_c)$, f_c is expressed as equation (2.17).

$$f_c \approx 1 + 0.5096\left(\frac{L^2}{g_o R_c}\right) + 0.0006347\left(\frac{L^2}{g_o R_c}\right)^2 \tag{2.17}$$

2.3.5 Revised M-TEST Models

Revised analytical M-TEST models based on the simulation results of this chapter are summarized in Table 2.3. Note, α_2 and ΔL are determined from FEM's.

V_{PI}		
Curled Cantilevers:	$V_{PI} = f_c V_{PI,\,IDEAL}$	see equation (2.17)
Stress-stiffened Fixed-Fixed Beams:	$V_{PI} = f_{ss} V_{PI,\,IDEAL}$	see equations (2.15) and (2.16)
Definition of Extracted Mechanical Properties		
Cantilevers:	$\frac{1}{\tilde{E}} = \frac{1}{E} - \frac{\upsilon^2}{E}\left[\frac{(w/L)^{1.37}}{0.5 + (w/L)^{1.37}}\right]^{0.98\,(L/t)^{-0.056}}$	
Fixed-fixed Beams:	$\frac{1}{\tilde{E}} = \frac{1}{E} - \frac{\upsilon^2}{E}\left[\frac{(w/L)}{0.18 + (w/L)}\right]^{1.77\,(L/t)^{-0.061}}$	
	$\tilde{\sigma} = \alpha_2 \sigma_o (1 - \upsilon)$	
Adjusted Geometry for Compliant Supports		
Cantilevers:	$L = L_{mask} + \Delta L$	
Fixed-fixed Beams:	$L = L_{mask} + 2\Delta L$	

Table 2.3: Summary of revised M-TEST models [64].

CHAPTER 3

Guidelines for Using M-TEST

Based on the theory developed in the previous chapter and the equipment requirements for M-TEST stated herein, the practical limits for designing and testing ideal test structures, and the guidelines for using M-TEST structures and for quantifying error bounds based on measured results are established in this chapter.

3.1 Equipment Requirements for M-TEST

Wafer-level probing of M-TEST structures is simple. Electrostatic measurements of the static pull-in voltage are made under an optical microscope (Nikon Measurescope UM-2) with long (> 5 mm) working length objectives. Magnetic micromanipulator probes (Quater Research & Development XYZ 300TL&R), a DC voltage supply (HP E3612A) and a voltmeter (HP 34401A) are needed for application and measurement of the pull-in voltage. The microscope is placed on a vibration-free platform and has a tilt-adjust stage for use with a differential interference objective. The stage is made from steel for the magnetic probers. For reference, the tilt-adjust stage blueprint is shown in Appendix B.

3.1.1 Pull-in Voltage Measurements

Three methods are used for observing pull-in. In one approach, a traditional normal-incident reflecting microscope, with either a Nomarski (Nikon BD Plan 5× DIC) or a differential interference (Nikon M Plan 10× DI) objective is used. This makes the sudden collapse after pull-in easy to observe, as shown in Figure 3.1.

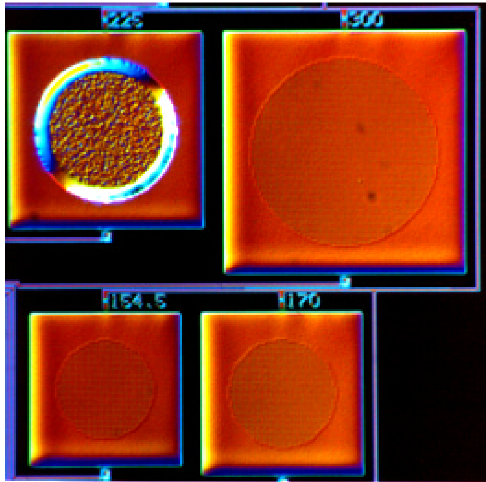

Figure 3.1: Nomarski DIC image of an electrostatically pulled-in aluminum diaphragm (top left) with initial gap g_o of 1.5 μm. (Devices courtesy of Phil Congdon at Texas Instruments.)

If the structures are thin and slightly transmissive at optical frequencies, an inexpensive multicoated wavelength (λ) filter in the light path shows changes in surface reflectivity of the structure as it deflects. Fringes appear between vertical distances on the surface greater than λ/2, as shown in Figure 3.2. As with the first approach, the sudden transition to pull-in is easy to observe as long as the displacement is more than λ/2. If required, these optical techniques can also be used to quantify deflections.

Since pull-in is also a switch closure if the structure collapses directly onto its opposing conductor, a simple circuit can be used to measure its change to a conducting state. A current-limiting resistor or a clipping current source is useful to avoid damaging the device. Alternatively, an HP 4145B Semiconductor Parametric Analyzer, if available, can be used. (Note, if this closed circuit is perfectly conducting, the device may lose all its stored charge and pop back up. However, because the short is typically resistive, a small voltage drop appears across the switch. Enough of an electrostatic force is developed across the narrow gap to keep the switch closed.)

As a rule of thumb, devices should be tested from the longest to the smallest, such that measured pull-in voltages go from low to high. This speeds up measurement since the previous measured pull-in voltage sets a practical lower limit for the next shortest length tested. More importantly, residual surface charges which can be left on an underlying dielectric layer under the structure after pull-in, scale with the applied voltage [65-66]. These charges propagate to adjacent structures and adversely affect the electrostatic force seen by them. At a given charge density, stiffer, shorter length structures are less affected than the longer. Obviously, less charge deposition is desired, and starting at lower voltages is one way to minimize the overall error that charging contributes to the measured pull-in

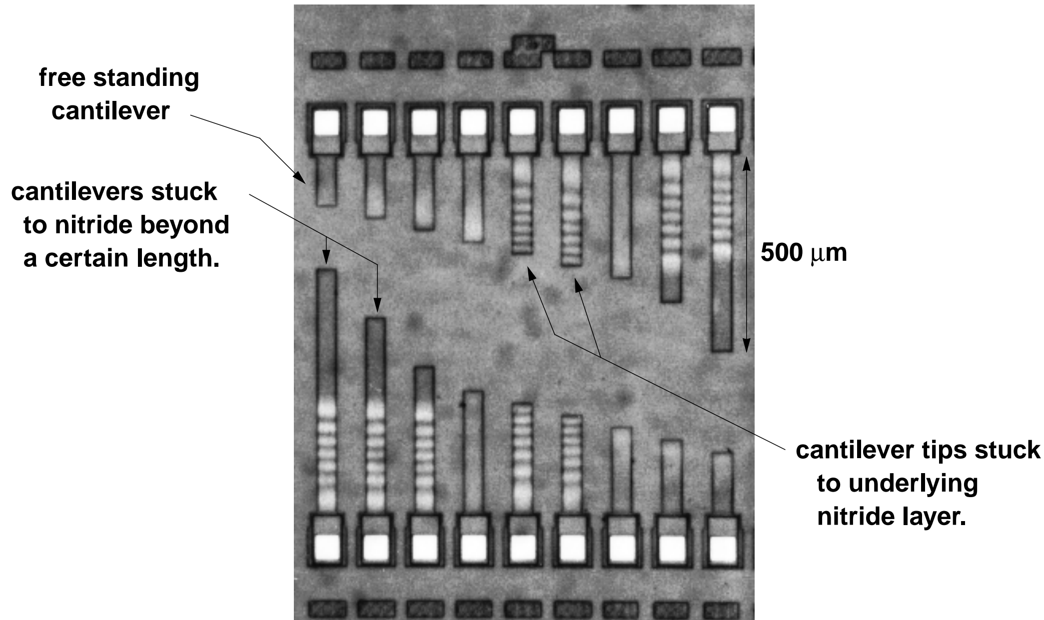

Figure 3.2: λ-filter (λ = 650 nm ±10 nm bandwidth) in the optical path of a microscope is used to observe vertical deflections in 2 μm-thick polysilicon cantilevers. Adjacent black-to-black fringes indicate a vertical distance of λ/2. Note, cantilevers are stuck down due to stiction problems.

voltages. These charges will eventually decay, but their time constant can be on the order of minutes or longer in atmosphere. Undocumented sources report that the decay can be accelerated by putting the devices under radiation [67].

3.1.2 Metrology Measurements

Accurate thickness, gap and length measurements are essential for reliable mechanical property extraction from almost any mechanical characterization method. For this purpose, three different metrological tools are used in M-TEST.

A properly calibrated Sloan Dektak IIA surface profilometer enables the measurement of the free-space gap under the structure and its thickness to a *precision* better than 1/1000th of a μm. The *accuracy* is limited by a scaling factor λ determined from the measurement of a thickness calibration standard with a stated accuracy of $\pm 5\%$. Examples of how the Dektak is used are shown in the next chapter. (See Figures 4.4 and 4.10) Capacitance measurements made on an HP 4280A are needed if the test structure is actuated over a gap that partly consists of a uniform dielectric separation layer. (For example, see Figure 4.9) The capacitance measurement estimates the dielectric thickness, i.e. the physical thickness of the film divided by its relative permittivity. The dielectric thickness is added to the free-space gap g_{fs} under the structure to estimate the total gap g_o. Lateral dimensional measure-

ments of length, width, and radius are made under an optical microscope using a calibrated Metronics Quadrachek II to accuracies of ± 0.5 μm.

3.2 Designing M-TEST Structures

As an *in-situ* monitor, M-TEST structures inherit gap and structural dimensions from the process used to fabricate the working sensors or actuators alongside. Two-dimensional layout control over lengths or radii allow tailoring their sensitivity to the mechanical properties of interest. In general, an *a priori* knowledge of the expected mechanical properties is useful to maximize sensitivity, but not necessary to extract mechanical properties. In the case where the properties are initially unknown, a single iteration with widely ranging M-TEST geometries, which accommodates large variations in mechanical properties, will reveal a reasonable bound on the expected mechanical properties for the subsequent iteration.

3.2.1 Selecting Layout Dimensions in Limiting Cases

In either the bending dominated limit ($S_nL^2/B_n \rightarrow 0$), or the stress dominated limit ($S_nL^2/B_n \rightarrow \infty$), where only S_n or B_n are desired, the selection of lengths for the M-TEST structures is simple. The equations in Table 2.1 can be used to approximate the required length or radius for a desired pull-in voltage based on expected mechanical property values and the specified gap and thickness.

The primary constraint in picking the appropriate voltage is the maximum limit of the DC voltage source and its observable resolution. Typical voltage sources supply up to 100 V, and good voltmeters accurately resolve 1 μV. Manual control of the voltage source dial, however, limits its repeatable accuracy to approximately 0.05% of full scale, which in the case for a 100 V scale is 0.05 V. Since the pull-in voltage scales as the square root of the stiffness, obtaining a 1% resolution in stiffness requires a 1/2% accuracy in voltage. This indicates that to obtain a 1% resolution in stiffness from a single pull-in device requires that its smallest pull-in voltage be above 10 V, if a 100 V source is used.

To avoid problems of stiction in the wet-etch release of longer length devices, shorter, higher pull-in voltage structures should be designed. The desire for smaller length devices is offset by the layout tolerance of the finest lithographic feature (typically 1 μm for surface micromachining) and the increasing influence of the support compliance. As a rule of thumb, structures 100 × longer than the smallest lithographic feature minimize geometry errors and allow approximating the offset in length correction (ΔL) for the support

compliance. If support compliance becomes a problem, i.e. $\Delta L \sim L$, clever layout techniques can be used to reduce it further [68].

To detect correlated errors and to minimize random errors, several lengths should be tested. Typically, the total number of distributed lengths should equal five times the number of parameters sought. For example, if only the Young's modulus is sought, five different lengths are adequate. The lengths should yield V_{PI}'s which are evenly spaced, where the maximum is several times the minimum. Note, in the bending dominated case, V_{PI} is quadratic with L, and in the stress dominated case, V_{PI} is linear. Beam widths w should be at least 10× the gap, so that the fringing field correction is valid. Furthermore, the L/w ratio should be chosen so that the effective modulus is constant or is very close to the Young's modulus. (See Figure 2.10, and equations (2.11) and (2.12))

3.2.2 Selecting Layout Dimensions for the General Case

Whenever two or more quantities are desired from the curve-fit of the M-TEST pull-in voltages, a centered design approach should be used [54].

If both the modulus and stress are desired from fixed-fixed beams or diaphragms, the center length or radius should be chosen so that $S_n L_{center}^2/B_n$ approximately equals $\pi^2/3$. In the compressive stress case, where S_n is negative, the center length or radius should be chosen far enough away from the buckling limit so that $S_2 L_{center}^2/B_2$ approximately equals $-\pi^2/12$. Furthermore the maximum length or radius L_{max} in the compressive stress case $S_n L_{max}^2/B_n$ should not be less than $-\pi^2/6$, because of the susceptibility to pre-buckled bending in the presence of compliant supports.

If both the modulus and its curling radius R_c are desired from cantilevers, a center length should be chosen such that the cantilever tip deflects only half of the nominal gap. This occurs when L_{center} is $(g_o|R_c|)^{1/2}$. Note, if R_c is negative, due to cantilevers curling toward the bottom electrode, an L greater than $L_{max} = (2g_o|R_c|)^{1/2}$, causes the tip to touch the bottom.

Careful selection of lengths will be based on the many of the practical considerations discussed in section 3.2.1. In the case of simultaneous modulus and stress extraction, L should be chosen to vary linearly for lengths greater than L_{center}, and to vary quadratically for lengths, smaller, so that the measured pull-in voltages will be evenly spaced. In the case of curled cantilevers, L should vary quadratically below L_{center}, and linearly above.

3.3 Mechanical Property Extraction using M-TEST

Although a single pull-in voltage measurement alone suffices in detecting chip-to-chip nonuniformity, extraction of the bending and stress parameters, B and S, respectively, from the pull-in voltage measurement versus several device lengths enables a quantification of device variations due to geometry and to mechanical properties, separates the effect of the bending and stress compliances, and reduces error.

Assuming ideal test structure geometry, a curve fit of the measured pull-in voltage versus length to the models in Tables 2.1 and 2.2, allows immediate extraction of B and S. However, if the structures have compliant supports, curl out of plane due to stress-gradients in cantilevers, or bow significantly due to compressive stress in diaphragms or fixed-fixed beams, finite-element models, careful measurement of geometry, or appropriate selection of data will be necessary before curve fitting to the revised models in Table 2.3, as explained in Chapter 2.

Once B and S are obtained and after the gap and thickness measurement, as directed in section 3.1, the mechanical properties can be extracted. The effective modulus $\tilde{E}$ is obtained by dividing B by $g_o^3 t^3$, and effective stress $\tilde{\sigma}$ is obtained by dividing S by $g_o t^3$. Note that $\tilde{E}$ and $\tilde{\sigma}$ are structure dependent. To obtain E, we make use of equations (2.11) and (2.12), for cantilevers and fixed-fixed beams, respectively, and for circular diaphragms by multiplying $\tilde{E}$ by $(1\text{-}\nu^2)$. The biaxial residual stress σ_o equals $\tilde{\sigma}$ for diaphragms, and equals $\tilde{\sigma}$ divided by $(1\text{-}\nu)$, for fixed-fixed beams. Note, S and $\tilde{\sigma}$ are zero for cantilevers which are free of residual stress. If unknown, ν can be obtained by algebra from either measuring the plate modulus from diaphragms and the Young's modulus from narrow beams or measuring the biaxial stress in diaphragms and the axial stress in fixed-fixed beams. For polysilicon, ν equal to 0.23 is a good approximation (Appendix A).

Note, the form of V_{PI} for a curved cantilever, as indicated in Table 2.3 and mentioned in section 3.2.2, allows simultaneous extraction of B and its curling radius R_c. Fixing either the known value of B or a very accurately measured value of R_c, can allow even better extraction accuracy of the other after curve fitting the measured pull-in voltages.

3.4 Estimating Error Bounds on Extracted Properties

Systematic and random errors in the measured quantities V_{PI}, L, R, t, and g_o, lead to errors in the extracted process parameters B and S, and mechanical properties $\tilde{E}$ and $\tilde{\sigma}$.

Systematic errors result from scaling or offset errors or from modelling errors, and manifest themselves in a well behaved manner across many tested samples. Random errors due to measurement imprecision obey gaussian distributions around expected values.

In the context of the revised M-TEST models, the goal of this section is to quantify the bounds of uncertainty on the extracted values of B, S, $\tilde{E}$ and $\tilde{\sigma}$, as a result of systematic and random errors in V_{PI}, L, R, t, and g_o.

3.4.1 Reducing Systematic Errors

Any systematic modeling errors must be eliminated before a meaningful error sensitivity analysis can made. Systematic errors, due to the neglect of the support compliance and the cantilever curvature in the ideal M-TEST models, are eliminated in the revised M-TEST models of Chapter 2. Similarly, the inclusion of plate effects for beams reduces systematic errors in varying width beams with the same thickness and length, and the inclusion of stress-stiffening due to variations in thickness and/or gap.

Systematic errors also occur from process-sensitive geometry or from scaling and offset measurement errors. For example, the length of a fabricated device may differ from the mask design either due to overetching a sacrificial layer that is part of a support, or due to lithographic offsets. These errors can be eliminated after a post-process measurement of geometry. Unfortunately, geometry and voltage measurements are also prone to systematic errors from offset or scaling problems in the measuring apparatus.

3.4.2 Equations from Statistics Theory

Two basic equations result from statistics theory which relate the errors in the measured parameters to propagated errors in an extracted quantity [49]. They are given in equations (3.1) and (3.2), for systematic errors and random errors, respectively, where the extracted quantity Q is a function of the independent parameters a, b, c, etc.

$$\delta Q = \frac{\partial Q}{\partial a}\delta a + \frac{\partial Q}{\partial b}\delta b + \frac{\partial Q}{\partial c}\delta c \cdots \tag{3.1}$$

$$\sigma_Q^2 = \left(\frac{\partial Q}{\partial a}\right)^2 \sigma_a^2 + \left(\frac{\partial Q}{\partial b}\right)^2 \sigma_b^2 + \left(\frac{\partial Q}{\partial c}\right)^2 \sigma_c^2 \cdots \tag{3.2}$$

The δ's in equation (3.1) represent systematic errors in the measured parameters a, b, c, etc. and in the extracted quantity Q. Likewise, the σ's in equation (3.2) represent the standard deviations of the random errors.

Random errors are averaged out when multiple beam lengths or diaphragm radii are tested. The standard deviation $\bar{\sigma}_Q$ of the extracted quantity after i measurements, is given in equation (3.3).

$$\frac{1}{\bar{\sigma}_Q} = \sum_i \frac{1}{\sigma_{Q_i}} \tag{3.3}$$

3.4.3 Error Analysis for Revised M-TEST Models in the Limiting Cases

The basic statistical equations are applied to pull-in voltage expressions derived from energy method calculations, neglecting fringing fields. The pull-in voltage expressions for cantilevers and diaphragms are functionally similar to equation (3.4) derived for a fixed-fixed beam, and are used to determine the effects on B, S, $\tilde{E}$ and $\tilde{\sigma}$, from errors in V_{PI}, L, R, t, and g_o.

$$V_{PI} = f c_{1n} \sqrt{\frac{B_n}{L^4}\left(c_{2n} + \frac{S_n L^2}{B_n}\right)} \tag{3.4}$$

The functional dependencies in equation (3.4) portray the more precise finite-difference calculations on which the revised M-TEST models are based, but are simpler to analyze. Note, B and S, and the constants c_1 and c_2 are structure dependent. f represents the effects of stress-stiffening, f_{ss} in fixed-fixed beams, or the effects of curling, f_c in cantilevers.

For cantilevers (n=1), which are stress-free, c_{11} equals 1.78×10^5 V/N$^{1/2}$, and c_{21} is one. For fixed-fixed beams (n=2), c_{12} equals 1.17×10^6 V/N$^{1/2}$, and c_{22} is $\pi^2/3$. For circular diaphragms (n=3), L is the radius, and c_{13} equals 5.10×10^5 V/N$^{1/2}$, and c_{23} is 1.2235.

In the bending dominated case, where $V_{PI} \propto f\,(B/L^4)^{1/2}$, and in the stress dominated case, where $V_{PI} \propto f\,(S/L^2)^{1/2}$, the application of equations (3.1) and (3.2) is simple [54]. For fixed-fixed beams and diaphragms in the bending dominated regime, the functional dependency of f_{ss} in comparison to other parameters of interest is weak, since C/ξ will be small (see equation (2.15)). Similarly, for cantilevers, when $L^2/(g_o R_c)$ is small, f_c can be neglected. In these limits, equations (3.5) and (3.6) are derived.

$$\begin{aligned} \delta B &\approx B\left(2\frac{\delta V_{PI}}{V_{PI}} + 4\frac{\delta L}{L}\right) \\ \delta \tilde{E} &\approx \tilde{E}\left(2\frac{\delta V_{PI}}{V_{PI}} + 4\frac{\delta L}{L} - 3\frac{\delta t}{t} - 3\frac{\delta g_o}{g_o}\right) \end{aligned} \tag{3.5}$$

$$\sigma_B \approx B\sqrt{4\left(\frac{\sigma_{V_{PI}}}{V_{PI}}\right)^2 + 16\left(\frac{\sigma_L}{L}\right)^2}$$

$$\sigma_{\tilde{E}} \approx \tilde{E}\sqrt{4\left(\frac{\sigma_{V_{PI}}}{V_{PI}}\right)^2 + 16\left(\frac{\sigma_L}{L}\right)^2 + 9\left(\frac{\sigma_t}{t}\right)^2 + 9\left(\frac{\sigma_{g_o}}{g_o}\right)^2} \tag{3.6}$$

Equations (3.7) and (3.8) are similarly derived for the stress dominated limit where f_{ss} is negligible.

$$\delta S \approx S\left(2\frac{\delta V_{PI}}{V_{PI}} + 2\frac{\delta L}{L}\right)$$

$$\delta\tilde{\sigma} \approx \tilde{\sigma}\left(2\frac{\delta V_{PI}}{V_{PI}} + 2\frac{\delta L}{L} - \frac{\delta t}{t} - 3\frac{\delta g_o}{g_o}\right) \tag{3.7}$$

$$\sigma_S \approx S\sqrt{4\left(\frac{\sigma_{V_{PI}}}{V_{PI}}\right)^2 + 4\left(\frac{\sigma_L}{L}\right)^2}$$

$$\sigma_{\tilde{\sigma}} \approx \tilde{\sigma}\sqrt{4\left(\frac{\sigma_{V_{PI}}}{V_{PI}}\right)^2 + 4\left(\frac{\sigma_L}{L}\right)^2 + \left(\frac{\sigma_t}{t}\right)^2 + 9\left(\frac{\sigma_{g_o}}{g_o}\right)^2} \tag{3.8}$$

3.4.4 Error Analysis for Revised M-TEST Models in the General Case

Ignoring the effects of f_{ss} in the general case for fixed-fixed beams and diaphragms, the errors in B and in S due to systematic errors are found to be coupled, as shown in equations (3.9).

$$\delta B \approx \left(\frac{2V_{PI}L^4}{c_1^2 c_2}\right)\delta V_{PI} + \left(\frac{4V_{PI}^2L^3}{c_1^2c_2} - \frac{2SL}{c_2}\right)\delta L - \left(\frac{L^2}{c_2}\right)\delta S$$

$$\delta S \approx \left(\frac{2V_{PI}L^2}{c_1^2}\right)\delta V_{PI} + \left(\frac{2V_{PI}^2L}{c_1^2} + \frac{2c_2B}{L^3}\right)\delta L - \left(\frac{c_2}{L^2}\right)\delta B \tag{3.9}$$

Equations (3.9) can be algebraically solved for errors in B and S, simultaneously. All other variables will be known. The errors $\delta\tilde{E}$ and $\delta\tilde{\sigma}$ can be determined by adding a $-3\tilde{E}(\delta t/t + \delta g_o/g_o)$ term, and $-\tilde{\sigma}(\delta t/t + 3\delta g_o/g_o)$ term to the rights of the equations for δB and δS, respectively.

The random errors in B and S for fixed-fixed beams and diaphragms are also coupled, as shown in equations (3.10).

$$\begin{aligned} \sigma_B^2 &\approx \left(\frac{2V_{PI}L^4}{c_1^2 c_2}\right)^2 \sigma_{V_{PI}}^2 + \left(\frac{4L^3 V_{PI}}{c_1^2 c_2} - \frac{2SL}{c_2}\right)^2 \sigma_L^2 + \left(\frac{L^2}{c_2}\right)^2 \sigma_S^2 \\ \sigma_S^2 &\approx \left(\frac{2V_{PI}L^2}{c_1^2}\right)^2 \sigma_{V_{PI}}^2 + \left(\frac{2V_{PI}^2 L}{c_1^2} + \frac{2c_2 B}{L^3}\right)^2 \sigma_L^2 + \left(\frac{c_2}{L^2}\right)^2 \sigma_B^2 \end{aligned} \tag{3.10}$$

The final case which is considered is that of curled cantilevers, where B is extracted based on a measured value of R_c and g_o, and f_c is approximated from equation (2.17) to be $(1 + 1/2\ L^2/g_oR_c)$.

$$\begin{aligned} \delta B \;\approx\; & 2\frac{V_{PI}}{c_1^2}\left(\frac{1}{L^2} + \frac{1}{2g_oR_c}\right)^{-2} \delta V_{PI} \;+\; \frac{4V_{PI}^2}{c_1^2 L^3}\left(\frac{1}{L^2} + \frac{1}{2g_oR_c}\right)^{-3} \delta L \\ & + \frac{V_{PI}^2}{c_1^2 g_o^2 R_c}\left(\frac{1}{L^2} + \frac{1}{2g_oR_c}\right)^{-3} \delta g_o \;+\; \frac{V_{PI}^2}{c_1^2 g_o R_c^2}\left(\frac{1}{L^2} + \frac{1}{2g_oR_c}\right)^{-3} \delta R_c \end{aligned} \tag{3.11}$$

$$\begin{aligned} \sigma_B^2 \;\approx\; & 4\frac{V_{PI}^2}{c_1^4}\left(\frac{1}{L^2} + \frac{1}{2g_oR_c}\right)^{-4} \sigma_{V_{PI}}^2 \;+\; \frac{16V_{PI}^4}{c_1^4 L^6}\left(\frac{1}{L^2} + \frac{1}{2g_oR_c}\right)^{-6} \sigma_L^2 \\ & + \frac{V_{PI}^4}{c_1^4 g_o^4 R_c^2}\left(\frac{1}{L^2} + \frac{1}{2g_oR_c}\right)^{-6} \delta g_o \;+\; \frac{V_{PI}^4}{c_1^4 g_o^2 R_c^4}\left(\frac{1}{L^2} + \frac{1}{2g_oR_c}\right)^{-6} \sigma_{R_c}^2 \end{aligned} \tag{3.12}$$

As the former equations indicate, the complexity greatly increases when multiple parameters are added to a curve fit. For other general cases, equation (3.4) can be used in combination with equations (3.1) and (3.2) to obtain the desired sensitivity parameters. Fortunately, most of the terms are either constants or are measured from structural geometry. The δ's and σ's, remain to be approximated. This will be shown by example in the following section.

3.4.5 A Numerical Error Sensitivity Example

Since M-TEST usually requires measurements of multiple beam lengths or diaphragm radii, random errors in B, S, $\tilde{E}$ and $\tilde{\sigma}$, which affect the *precision* of the extracted quantities, will be averaged out, as shown by equation (3.3), and will be negligible compared to systematic errors, which affect the *accuracy*, and result from inaccurate measurements of the geometry or the pull-in voltage.

Systematic variations in the measured thickness t can be represented as $(1+\Delta t)\lambda_t t_N$, where t_N is the nominal thickness, Δt is the actual thickness minus the nominal thickness plus measurement offsets divided by the actual thickness, and λ_t is the measurement scaling error in thickness. Similarly, the measured gap g_o, pull-in voltage V_{PI}, and length L are represented by $(1+\Delta g_o)\lambda_g g_N$, $(1+\Delta V_{PI})\lambda_{PI} V_N$, and $(1+\Delta L)\lambda_L L_N$, respectively.

As a numerical example, consider a polysilicon cantilever (E = 163 GPa) nominally 250 μm long, 2 μm thick, and with a 2 μm gap, having an estimated pull-in voltage of 9.20 V. Assume that all Δ's are zero, since they can be easily detected and corrected, and only measurement scaling errors (λ's) exist, where λ_t and λ_g are 0.99 and λ_{PI} and λ_L are 1.01. Based on these errors, $\delta B/B$ will be $(1-\lambda_{PI}^2\lambda_L^4)$, which from equation (3.5) is approximately 6%, and $\delta E/E$ will be $(1-\lambda_{PI}^2\lambda_L^4\lambda_t^{-3}\lambda_g^{-3})$, which is approximately 13%.

These calculations indicate a very strong sensitivity to geometry, which can be a limiting factor in using M-TEST for mechanical property extraction. Nevertheless, if a user of M-TEST is more interested in fabrication problems in geometry this limitation becomes an advantage, as illustrated by a practical example in section 4.1.

Often it is useful to compare the nominal values B_N and S_N to extracted values of B and S after removing fabrication variations in geometry. For this purpose, B_{new} and S_{new} are defined as follows. They equal $B/((1+\Delta g_o)^3(1+\Delta t)^3)$ and $S/((1+\Delta g_o)^3(1+\Delta t))$, respectively. These definitions will be used in section 4.3.

CHAPTER 4

Experimental Results

Revised M-TEST models developed in the previous chapter will be used to demonstrate: (1) assessment of process integrity in silicon wafer-bonded MEMS devices by determining the bending- and stress- process parameters, *B* and *S*, (2) mechanical property extraction from *B* and *S* for polysilicon surface-micromachined MEMS test structures, following careful measurement of device geometry, and (3) monitoring inter-run and intra-run variation of *B* and *S*, and of mechanical and geometrical properties for polysilicon MEMS.

4.1 M-TEST Assessment of MEMS Process Integrity

The dependence of *B* and *S* to cubic or quadric powers of thickness *t*, gap g_o, and length *L*, makes them a sensitive monitor of variation in geometry when mechanical properties are structure-independent. This is the case when monitoring gap variations in single-crystal silicon wafer-bonded test structures released by plasma over-etching. Parallel and adjacent, narrow and wide fixed-fixed beams yield two very different B_2's. While the B_2 from the wide beams confirms expected Young's modulus value of single-crystal silicon, the B_2 from the narrow beams with the same modulus, acts a monitor for plasma over-etching [22].

4.1.1 Process Description

Fixed-fixed beam test structures designed for a nominal thickness of 14.5 μm and a gap of 1.0 μm are fabricated with their length axis in the [110] direction of <100> single-crystal silicon using MIT's sealed-cavity wafer-bonded technology [28]. Since the structures are

thick in comparison to their gap and have a planar geometry, ideal two-dimensional M-TEST models are applicable. Also, because these wafer-bonded structures have relatively low residual stress [23], the stress parameter S_2 is small and does not contribute to mechanical stiffness. In this limit, the bending-dominated analytic form for the pull-in voltage V_{PI}, which is found in Table 2.1 and repeated below in equation (4.1), is used.

$$V_{PI} = \sqrt{\frac{11.86\, B_2}{\varepsilon_o L^4 \left(1 + 0.42\, g_o / w\right)}} \tag{4.1}$$

4.1.2 Measurements of Pull-in Voltage and Geometry

Figure 4.1 shows the measured pull-in voltage versus length for two sets of parallel and adjacent fixed-fixed beams fabricated by this process with nominal widths of 10 μm and 50 μm. When the data are fit to equation (4.1), the B_2's can be determined to better than 10%. For the 50 μm-wide beams, B_2 equals 5.6×10^{-22} Pa-m^6, and is close to the nominal value of 5.2×10^{-22} Pa-m^6 based on the nominal geometry and an E of 169 GPa in the [110] direction of single crystal silicon [48]. B_2 equal to 10.0×10^{-22} Pa-m^6 for the 10 μm-wide beams is twice as large. This discrepancy suggests a problem with the geometry for the 10 μm-wide beam.

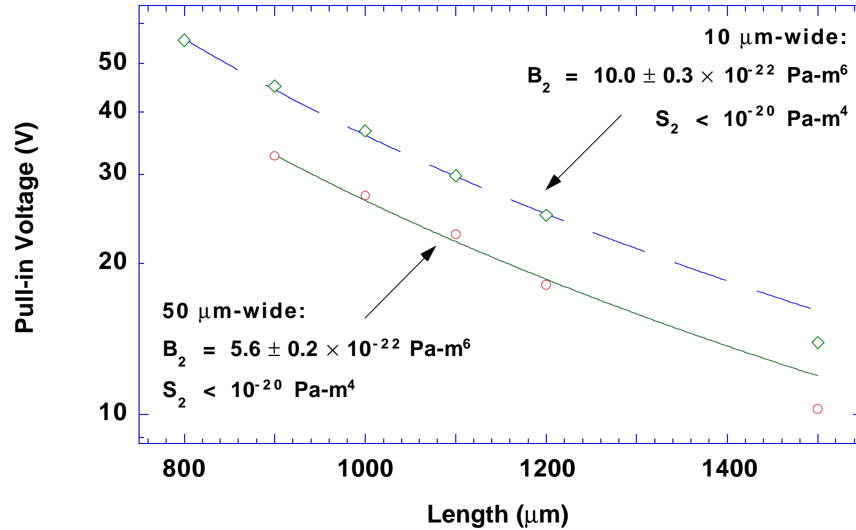

Figure 4.1: Experimental pull-in voltages (points) vs. fixed-fixed beam length. Fitted lines are obtained from closed-form expressions for ideal test structures. Nominal B_2 value is 5.2×10^{-22} Pa-m^6.

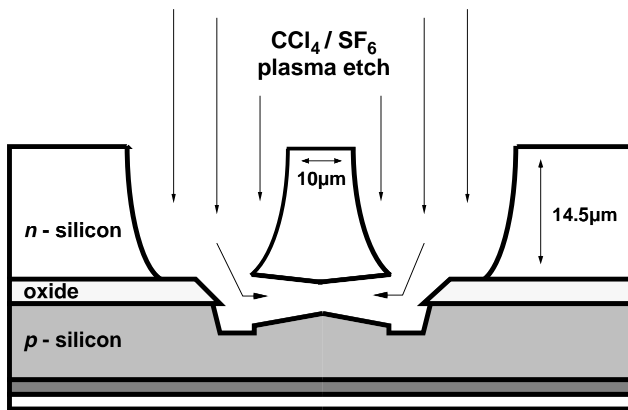

Figure 4.2: Illustration shown in lateral cross-section, of plasma attacking the underside a narrow (nominally, 10 µm-wide and 14.5 µm-thick) wafer-bonded beam during its release. Etch profiles and dimensions are exaggerated for clarity.

One possible explanation is an over-etch resulting from a prolonged anisotropic CCl_4/SF_6 plasma-etch release of the microstructures. This idea is illustrated in Figure 4.2, where etched dimensions are magnified for clarity. The over-etch is expected to have a limited encroachment under the beam. Therefore, the overall gap under narrow beams will be more affected than the gap for wide beams. This is shown in SEM cross-sections of a 10 µm- and 50 µm-wide cantilever in Figure 4.3. Both beams are positioned above substrate landing pads. Although there is an observable over-etch of the *p*-silicon substrate pads, the *n*-silicon beam undersides remain unaffected and are relatively flat.

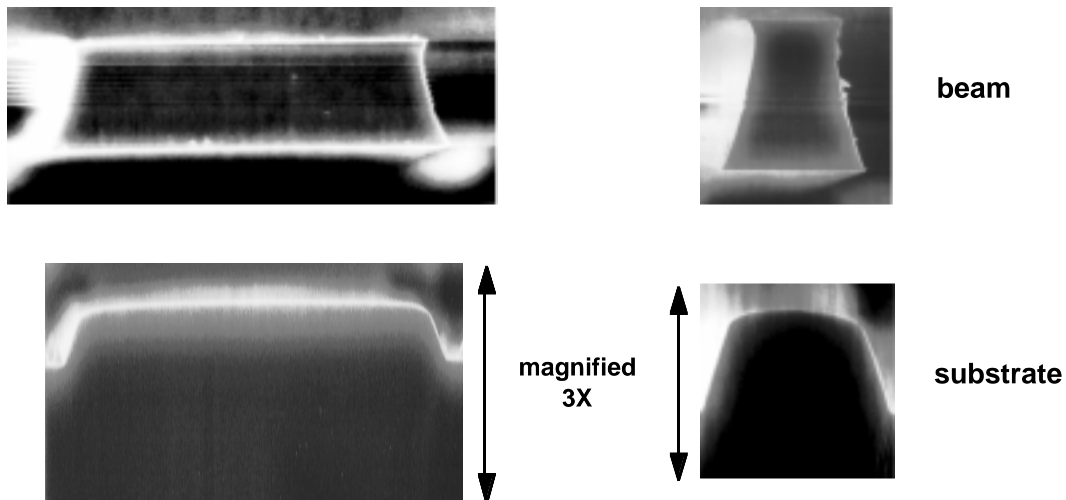

Figure 4.3: SEM cross-sections of 50 µm- (left) and 10 µm-wide (right) cantilevers over corresponding substrate landing pads. The width of 10 µm-wide beam underside is 17 µm. Its substrate landing pad width is approximately 15 µm. The rounding of the 15 µm-wide pad is approximated by a radius of curvature of 60 µm. Note the relative flatness of the beam undersides in comparison to the substrate.

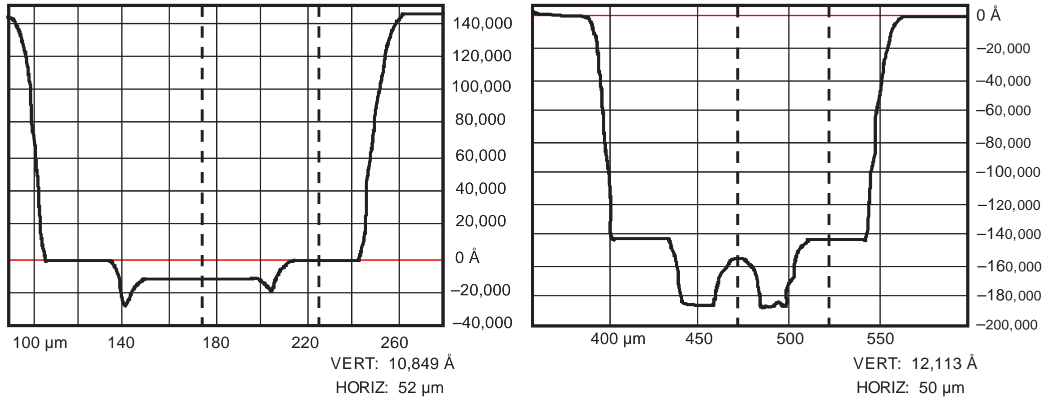

Figure 4.4: Dektak surface profilometry measurements of *p*-substrate contacts of a 50 µm (left) and 10 µm (right) fixed-fixed beam. The dotted lines align vertical height differences of the center of the pads to the top of the exposed oxide. This difference, the minimum gap, is 1.08 µm and 1.21 µm, respectively. (Vertical scale is in Å with ± 10Å accuracy, and horizontal in µm.)

Figure 4.4 shows Dektak surface profile measurements using a 12.5 µm diamond radius tip across a 10 µm- and a 50 µm-wide beam substrate pad and trench regions. The dotted lines align differences in height between the top of the oxide and the center of the substrate pads, to a vertical resolution of 10 Å. This distance is the minimum gap between the bottom of the beam and center of the pad, and is 1.08 µm for the 50 µm-wide beam and 1.21 µm for the 10 µm-wide beam. They show only a 50 Å variation along the beam length. Profilometer measurements also indicate a uniform thickness of 14.37 µm of the mechanical layer across the wafer.

The SEM photos in Figure 4.3 are used to obtain an effective radius of curvature R_s of the pad regions along the beam width. R_s is 60 µm (± 5%) for the 10 µm-wide beam. There is significantly less curvature for the wider beam, and hence the gap g_o is assumed to be uniformly 1.08 µm. From the SEM, the 10 µm-wide beam has a 10 µm width w_t on the top and a 17 µm width w_b on the bottom. For the analyses to follow, the 10 µm-wide beams are assumed to have a trapezoidal cross-section based on w_t and w_b, as shown in Figure 4.5.

4.1.3 Analysis of Results

Because of the well-defined geometry of the 50 µm-wide beams, pull-in results from these beams have been used to confirm that an E of 169 GPa can be determined from the M-TEST models [23, 54]. Based on B_2, g_o, and t, reported above, M-TEST results yield $\tilde{E}$ = 173 GPa, with a ± 13 GPa error bound determined primarily by the scatter of the measured data. For the beam geometries tested, the extracted $\tilde{E}$ is expected to be within

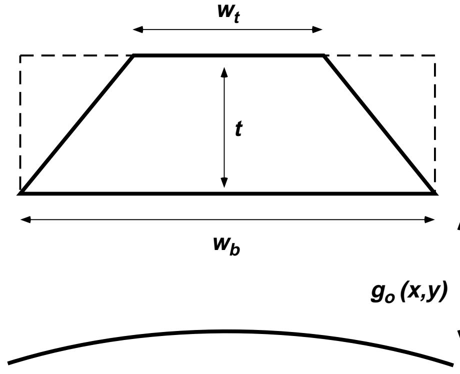

Figure 4.5: Schematic cross-section approximating the plasma over-etched 10 µm-wide narrow beam geometry. V_{PI} is calculated from an analytical M-TEST model and a 2D finite-difference model using this geometry.

0.5% of E, based on equation (2.12) and Figure 2.8. An upper bound determined for the residual stress, $\sigma_o(1-\nu) < 10$ MPa, is based on the tolerance of the curve fitting routine [54].

The electrostatic and mechanical forces in the M-TEST models are adjusted for the rounded gap and the approximate trapezoidal cross-section of the 10 µm-wide beams to show that B_2 is correctly determined from their geometry and known Young's modulus. Because the electrostatic force is proportional to the inverse of the gap squared, an effective uniform gap g_{eff} is estimated for pull-in geometries across any parallel deforming cross-sections, using equation (4.2), where the x- and y-axes are in the plane of the chip.

$$g_{eff} = \left[\frac{1}{A} \int_A \frac{dx\,dy}{g_o(x,y)^2} \right]^{-1/2} \tag{4.2}$$

Based on a 15 µm-wide rounded substrate pad with $R_s = 60$ µm, a g_{eff} equal to 1.39 µm is calculated. This effective gap is inserted into the equation for B_2 in place of g_o. The compliance of the beams' trapezoidal cross-section and the electrostatic force on the bottom face of the beam are included by scaling B_2 by the ratio of the moment of areas between the beams' trapezoidal cross-section to an equivalent rectangular beam whose width is given by w_b. (See Figure 4.5) The equation for B_2 is then updated as shown in equation (4.3).

$$B_2 = \tilde{E} t^3 g_{eff}^3 \left(\frac{w_t^2 + 4 w_t w_b + w_b^2}{3 w_b (w_t + w_b)} \right) \tag{4.3}$$

Using an $\tilde{E}$ of 169 GPa, equation (4.3) gives a B_2 equal to 10.5×10^{-22} Pa-m^6, which is very close to the measured value of 10.0×10^{-22} Pa-m^6. When this calculated value of B_2 is used in equation (4.1), the pull-in voltage can be predicted. As a test case, consider the 10 µm-

wide and 1000 μm-long fixed-fixed beam. Based on the calculated value of B_2, V_{PI} is estimated to be 36.6 V, which is close to the measured value of 35.9 V.

4.1.4 Accurate Modeling in Two- and Three-Dimensions

Due to potentially small errors in overlap between the fit of equation (4.1) to results derived from the numerical two-dimensional (2D) simulation of ideal test structures, and to the approximation in gap for the beam geometry allowing the use of equation (4.1), better pull-in voltage predictions are expected by more precise numerical techniques. Therefore, as an example, pull-in behavior of the 10 μm-wide and 1000 μm-long fixed-fixed beam is analyzed using a 2D finite-difference model with fringing-field correction, where the gap under zero bias is assumed to be uniformly g_{eff}. Full three-dimensional (3D) simulations are also performed using CoSolve-EM [69], and have a carefully rendered rounded substrate pad. A minimum gap of 1.21 μm together with a radius of curvature of 60 μm are used for the substrate pad geometry, as shown in Figure 4.6.

The calculated pull-in voltages are 36.5 V and 36.3 V from the 2D and 3D models, respectively, and agree closely with each other, and with the experimental value of 35.9 V. For the 3D simulation, a mesh-convergence study showed that the mechanical stiffness of the meshed beam and the electrostatic forces are calculated within about 5% error, and since the pull-in voltage goes approximately as the square root of the stiffness, pull-in errors resulting from the mesh are of order 2.5%. A similar analysis showed that the 2D meshed errors are less than 1%. Figure 4.7 shows the calculated deflection at the beam center as a function of voltage.

The small remaining discrepancy between simulation and experiment may result from assuming a trapezoidal cross-section and ideal fixed-ends, both of which will result in

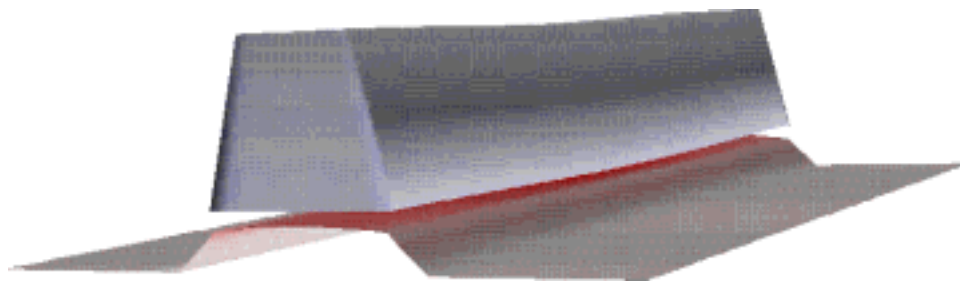

Figure 4.6: A deformed geometry of a nominal 10 μm-wide fixed-fixed beam under electrostatic loading using MEMCAD. The beam is 14.37 μm-thick, and it is 10 μm-wide on the top and 17 μm-wide at the bottom. The radius of curvature of the rounded ground plane is 60 μm. The axis along the 1000 μm beam length is scaled 1/10 for better viewing.

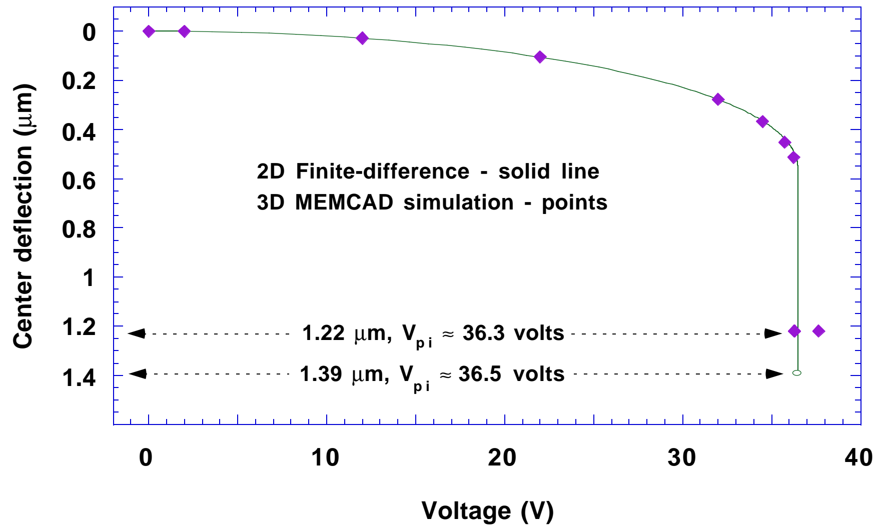

Figure 4.7: Comparison of 2D and 3D coupled electromechanical simulation for pull-in of 1000 μm-long narrow beam example. Note, deflections are coincident between the uniform gap structure in 2D and rounded-gap structure in 3D.

slightly stiffer structures and higher pull-in voltages than the actual devices. Nevertheless, B_2 from narrow beams quantitatively determines effective changes in geometry reasonably well, and is consistent with results from the analytical M-TEST models.

4.2 M-TEST Mechanical Property Extraction from Polysilicon

Revised M-TEST models in Table 2.3 are used in combination with techniques for accurate geometric measurement of thickness and gap to demonstrate mechanical property extraction from relatively thin surface-micromachined polysilicon test structures. Pull-in voltages from cantilevers (n = 1) and fixed-fixed beams (n = 2) determine both the Young's Modulus E and the uniaxial residual stress $\sigma_o(1\text{-}\nu)$ from B_n, S_n, t, and g_o. (In principle, B_3 and S_3 from circular diaphragms (n = 3) allow independent extraction of E, σ_o, and ν. However, the practice of placing sacrificial release etch holes in surface-micromachined circular diaphragms modifies structural properties, and requires complex modeling beyond the scope of this thesis. Nevertheless, such modeling is currently in progress [70].) The sensitivity of M-TEST to residual stress is also demonstrated by observing that the simple placement of the MEMS test chip on the vacuum chuck of a probe station can significantly affect the pull-in voltage.

4.2.1 Test Structure Fabrication

Cantilever and fixed-fixed beam test structures of 40 μm widths and of varying lengths are fabricated on a 1 cm^2 chip from conformally-deposited fine-grain polysilicon (LPVCD at 580 ºC) using the surface-micromachining technology of the Multi-User MEMS Processes (MUMPs) at the Microelectronics Center of North Carolina (MCNC) [27]. Fabricated devices from MUMPs 5 are shown photographed in Figure 4.8. They have a nominal 2 μm thickness t and a free-space gap g_{fs}, which is created from a nominal 2 μm-thick sacrificial oxide release. Released cantilever structures are shown schematically, as ideally uncurled, in 3D in Figure 2.4, and in a 2D cross-section in Figure 4.9. The nitride layer, which has a nominal thickness as deposited of $t_{SiN} = 0.5$ μm, is used to dielectrically isolate the substrate from the anchor of the mechanical devices.

Surface profilometry reveals the actual thickness and free-space gap of the MUMPs 5 test chip. In Figure 4.10, a calibrated Dektak 8000 measurement made by a 9 μg-force contact scanning across the length of a released cantilever measures a t of 2.10 μm, and a g_{fs} of 2.34 μm, with less than ± 0.03 μm surface variation. A capacitance measurement between a base polysilicon layer directly on top of an unetched nitride region and the silicon substrate (see Figure 4.9) yields a dielectric thickness, $t_{SiN}/\varepsilon_{SiN}$, equal to 670 Å, where ε_{SiN} is the relative nitride permittivity at 1 MHz. Based on a nominal thickness 0.5 μm for t_{SiN}, ε_{SiN} is determined to be 7.

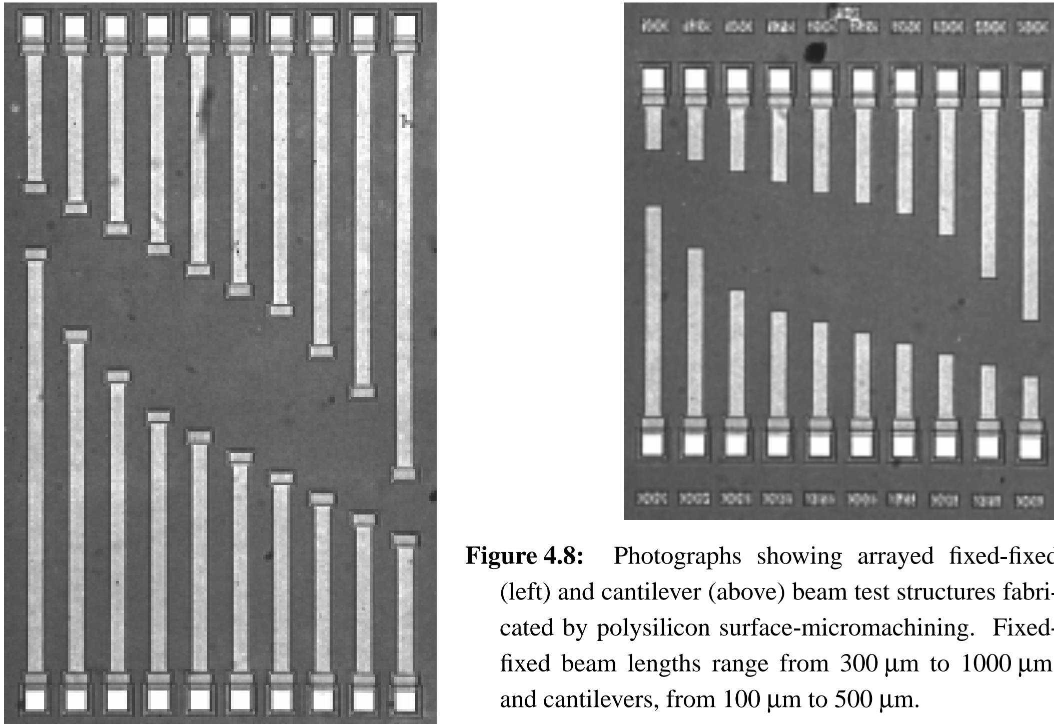

Figure 4.8: Photographs showing arrayed fixed-fixed (left) and cantilever (above) beam test structures fabricated by polysilicon surface-micromachining. Fixed-fixed beam lengths range from 300 μm to 1000 μm, and cantilevers, from 100 μm to 500 μm.

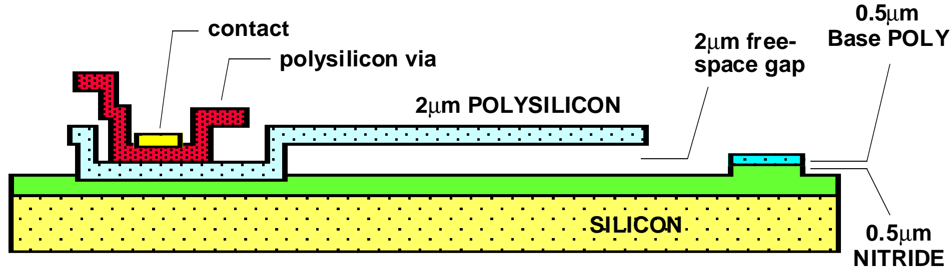

Figure 4.9: Schematic cross-section of polysilicon surface-micromachined cantilever, showing nominal thickness and gap geometries. Note the over-etch of the nitride dielectric isolation layer due to plasma over-etching of removed base polysilicon and oxide layers. The polysilicon via for the contact is an artifact of the processing and is structurally insignificant. Vertical dimension are exaggerated for clarity.

Since the nitride layer also acts as an etch-stop, it becomes over-etched in the process of ensuring complete removal of any patterned overlaying polysilicon or oxide layers. Under the movable part of the beam, the nitride is over-etched by Δt_{SiN1} by a Cl_2-based reactive ion etch (RIE) to remove the base polysilicon layer. Under the anchor region of the beam, the nitride is over-etched by $\Delta t_{SiN1} + \Delta t_{SiN2}$, from the removal of both the base polysilicon layer and the first sacrificial oxide layer, where Δt_{SiN2} results from the oxide over-etch by a F_2-based RIE. As shown in Figure 4.10, Δt_{SiN2} is determined to be 0.11 µm from the difference in height between the tops of the polysilicon anchor region and of the pushed-down beam. Since there is no direct way to measure Δt_{SiN1} using profilometry, the foundry specified value of Δt_{SiN1}, stated to be less than 100 Å, is used [27].

Finally, the electrostatic gap g_o, for use in M-TEST, is calculated as the sum of g_{fs} and $(t_{SiN} - \Delta t_{SiN1})/\varepsilon_{SiN}$ and equals 2.40 µm. The mask-drawn length of the devices are modified by the addition a ΔL/support to account for the bending compliance of the support. For nominal values of thickness and free-space gap, ΔL is determined to be 5.85 µm from FEM simulations, as discussed in section 2.3.3.

Cantilevers curl out of plane due to stress-gradients through the polysilicon film thickness. A optical tip deflection measurement is used to determine the curling radius R_c of 40 mm ± 0.3 mm from the 500 µm-long cantilever. This value of R_c is consistent with the curling radii of other cantilevers made from the same polysilicon layer, based on assuming a non-varying in-plane stress profile in the film.

4.2.2 Pull-in Voltage Measurements

Pull-in voltage measurements are taken from curled cantilevers for mask-drawn lengths of 100 µm to 500 µm. For comparison, the theoretically determined pull-in voltage for

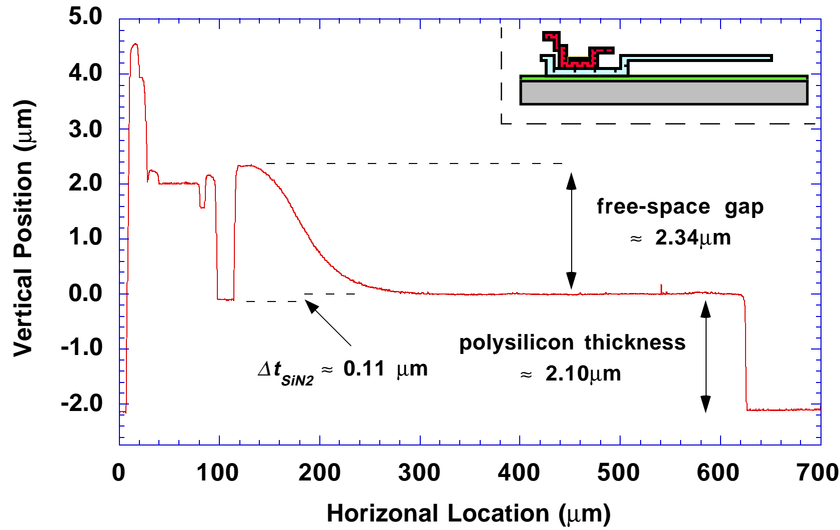

Figure 4.10: Dektak surface profilometry of a cantilever similar to the one shown in the inset, reveals the polysilicon and spacer-oxide thicknesses. An ~9 μg force is applied at the tip of the scanning probe, pushing the cantilever down until it touches the nitride layer. The nitride over-etch due to the oxide over-etch creating the beam anchor is Δt_{SiN2}.

similar dimensioned, but uncurled, cantilevers are plotted alongside the measured data, as shown in Figure 4.11. As expected, the measured and theoretical values deviate for larger values of length where the gap becomes significantly non-uniform. However, with a measured value of R_c, t, and g_o, and with a curve fit of the measured data to the revised M-TEST model including ΔL, an $\tilde{E}$ of 153 GPa is obtained. Results from equation (2.11) and Figure 2.7 indicate that $\tilde{E}$ is within 1% of E for all of the lengths tested with $\nu = 0.23$, so that $E \approx \tilde{E}$. Using this value of E, a linearly-varying approximation of the stress-gradient needed in the unreleased cantilevers to obtain an R_c equal to 40 mm, equals E/R_c, or 4 MPa/μm.

Pull-in voltage measurements from fixed-fixed beams for mask-drawn lengths of 300 μm to 700 μm, are shown in Figure 4.12. Fixed-fixed beams longer than 700 μm bow away from the substrate due to pre-buckled bending. For very large beam lengths, beyond the ideal fixed-fixed beam Euler-buckling limit ($S_2L^2/B_2 < -\pi^2/3$), the center deflection can be many times the nominal gap. Because this highly nonlinear behavior found in beams longer than 700 μm is difficult to predict and model, these beams are not tested. The V_{PI}'s of smaller length beams, however, are used to extract mechanical properties. Revised M-TEST models for the tested beam geometries indicate that $E \approx \tilde{E}$ equals 157 GPa, based on equation (2.12) and Figure 2.8, and that $\tilde{\sigma} = \alpha_2\sigma_o(1\text{-}\nu) = -3.8$ MPa, which approximately equals $\sigma_o(1\text{-}\nu)$, since $\alpha_2 \approx 1$ based on FEM's as discussed in section 2.3.3.

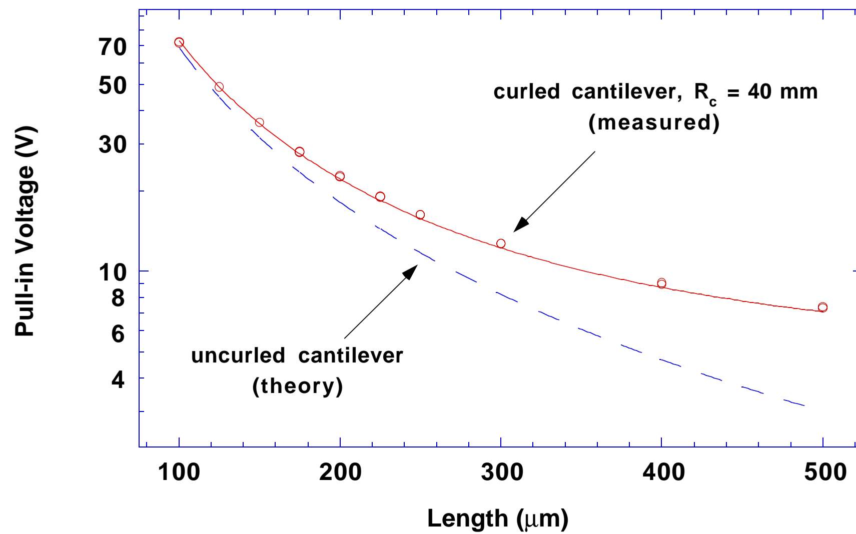

Figure 4.11: Theoretical and measured V_{PI}'s for uncurled (dashed line) and curled cantilevers (data points), compared. Data fit to revised M-TEST models (solid line), based on a measured R_c.

Additional compressive stress from substrate deformation on a vacuum probe station as schematically illustrated in Figure 4.13, decreases the critical length for the onset of pre-buckled bending. Its effect on the pull-in voltage can be seen alongside the previous "no-vacuum" data in Figure 4.12. In beams 500 µm and longer, large bowing is observed, and

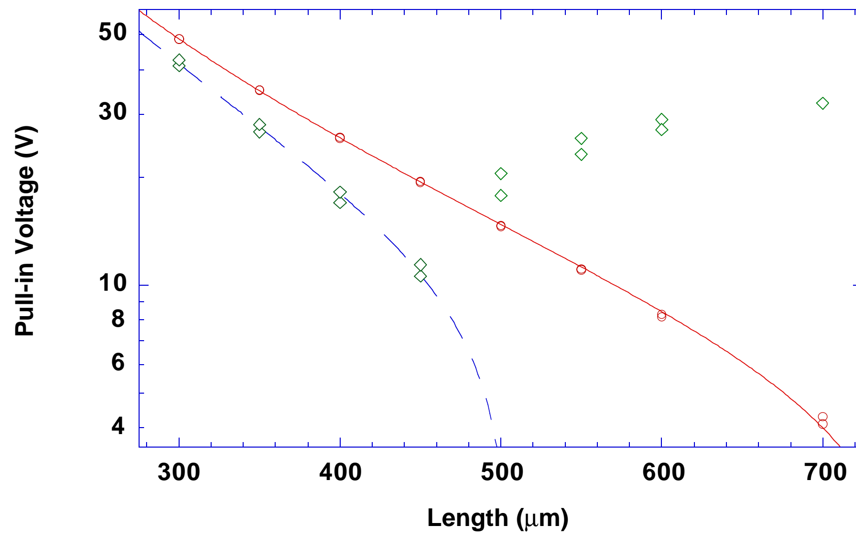

Figure 4.12: Measured V_{PI}'s (circles) from fixed-fixed beam structures fit to revised M-TEST models (solid-line). A fit (dashed-line) of measured V_{PI}'s (diamonds) after vacuum application on wafer-chuck reveals more than a doubling in stress. Beams 500 µm and longer are bowed or buckled, and are not included in the dashed-line fit. See Figure 4.13 for a schematic interpretation.

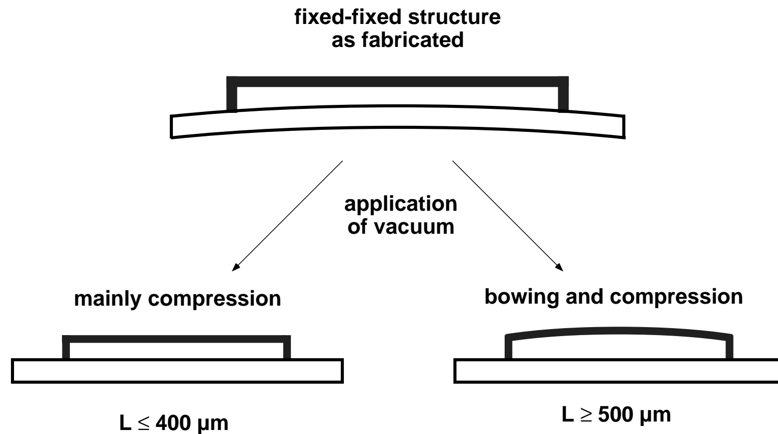

Figure 4.13: Schematic illustrating substrate deformation and its effects on stress in fixed-fixed structures. L = 450 µm shows a tri-state behavior as explained in the text.

the pull-in voltage is discontinuous from that at 450 µm. For the 450 µm-long beam, a tristate behavior is observed. At voltages below pull-in, the beam which begins slightly bowed up, pulls-through to a second state in which it is slightly bowed down, and then continuously deforms until it pulls-in. In beams longer than 450 µm, the pull-through voltage is synonymous with the pull-in voltage, and at shorter lengths the pull-through voltage is not observed. Taking pull-in data from beams shorter than 500 µm, the new axial stress state can be determined. With an $\tilde{E}$ determined earlier of 157 GPa, $\tilde{\sigma}$ is found to be more than twice its no-vacuum value, and approximately equals 9 MPa.

4.3 M-TEST Monitoring of Inter-Run and Intra-Run Variations

M-TEST data taken from several MUMPs die from within a specific fabrication run and across different runs allows a comparison of processing variations due to mechanical properties and geometry.

4.3.1 Data from Cantilevers and Fixed-fixed Beams

A semilog scatter plot of the extracted B_1 and $1/R_c$ from the MUMPs cantilevers is shown in Figure 4.14. The measured values of $1/R_c$, which are at best accurate to ± 0.8 m^{-1} from the optical tip deflection measurement of a 500 µm-long cantilever using a λ-filter at 650 nm, agree to within ± 1 m^{-1} of the extracted $1/R_c$'s, whose accuracy scales linearly with the accuracy in L^2 and inversely with the accuracy in g_o. L is known to better than 1%, and

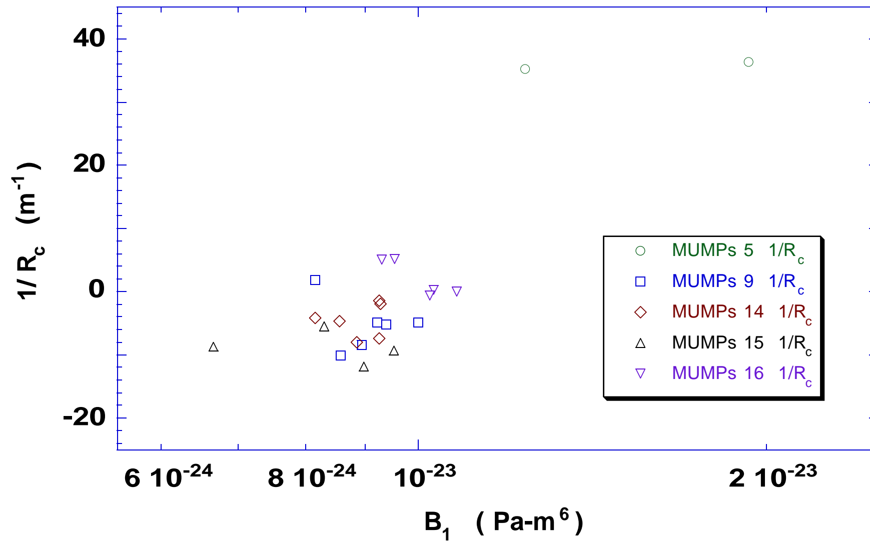

Figure 4.14: Semilog scatter plot of $1/R_c$ versus B_1 for M-TEST cantilever data taken from each die (individual points) across several MUMPs process runs, labelled by number. The gap g_o is assumed to be 2.07 µm. The extracted $1/R_c$ is accurate to within ±1 mm^{-1}, by a comparison to optical cantilever tip deflection measurements.

g_o is assumed to be the nominal value of 2.07 µm from a g_{fs} of 2 µm and nitride dielectric thickness of ~700 Å. Dektak measurements indicate that g_o can vary by up to 10% around the nominal value. Obviously, the accuracy of $1/R_c$ is limited more by g_o than by L, can be scaled appropriately to the actual value once g_o is measured.

A similar log-log scatter plot of the extracted S_2 and B_2 from the MUMPs fixed-fixed beams is shown in Figure 4.15. The negative values of S_2 indicate that all the beams are fabricated in compressive residual stress.

4.3.2 A Comparison of the Results

A comparison of B_1 and B_2 in Figure 4.16 indicates excellent agreement for almost all dies. This agreement from two very different structures indicates that the *precision* in B_1 and B_2 is very good and lends credibility to the M-TEST models. The small average ratio $\langle B_2/B_1 \rangle$ of 1.03, suggests a residual modeling error, which is possibly due to the neglect of fringing fields at the tip of the cantilever. The extracted B's vary widely, and are on average ($\overline{B}_2 = 9.4 \times 10^{-24}$ Pa-m^6 ± σ of 2.6×10^{-24} Pa-m^6) below the nominal expected value B_N of 1.16×10^{-23} Pa-m^6, where g_o is 2.07 µm, t is 2 µm and E is 163 GPa.

The variations in the extracted B should be reduced significantly if correlated variations in geometry are eliminated. (Note that E is not expected to vary more than 10% around its

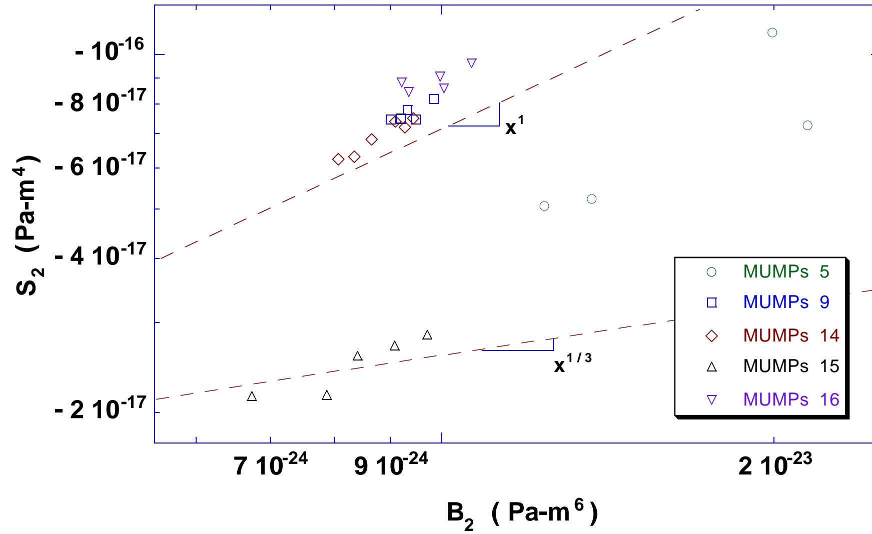

Figure 4.15: Log-log scatter plot of S_2 versus B_2 for M-TEST fixed-fixed beam data taken from each die (individual points) across several MUMPs process runs, labelled by number. Note, the $t^3 g_o^3$ and $t g_o^3$ dependency of B_2 and S_2 can be seen through the mechanical property variations in E and $\sigma_o(1\text{-}\nu)$, and indicates that the geometric variations in g_o and t have a strong effect on B_2 and S_2. The x^1 and $x^{1/3}$ curves represent the expected variation in S_2 versus B_2, when either the gap or the thickness varies, respectively, while the other is constant.

nominal polysilicon value of 163 GPa, even in the presence of strong out-of-plane texture [Appendix A].) Dektak IIA and nitride capacitance measurements are used to calculate $B_{2,new}$ and $S_{2,new}$ for the fixed-fixed beams, following the procedure in section 3.4. A log-log scatter plot, having the same vertical and horizontal dynamic range as Figure 4.15, is shown in Figure 4.17. As expected, a much tighter distribution in $B_{2,new}$ as compared to B_2, is found. The average value $\overline{B}_{2,new}$ over the 24 samples is $1.27 \pm 0.10 \times 10^{-23}$ Pa-m^6, with a probable error of the mean ($\sigma_{N=24}$) of $\pm 0.02 \times 10^{-23}$ Pa-m^6, or 1.7%. Using $\overline{B}_{2,new}$ an E of 178 ± 3 GPa is determined. This value appears large. See Chapter 5 for a discussion and comparison with other reported results.

The variation in $S_{2,new}$ is quite broad indicating a large inter-run residual stress variation, but a much smaller intra-run variation. This suggests that the fabrication process very noticeably changes the stress conditions in the polysilicon from run to run (typically spaced apart by four months), but that within a run this variation is small, as would be expected from variations in anneal conditions and doping levels. The average intra-run standard deviation in $S_{2,new}$ is less than 10%. However, the average $\overline{S}_{2,new}$ from each run varies from -3.27×10^{-17} Pa-m^4 for MUMPs 15 to -1.05×10^{-16} Pa-m^4 for MUMPs 16, indicating an equivalent residual stress $\sigma_o(1\text{-}\nu)$ variation from -1.8 MPa to -5.9 MPa, respectively.

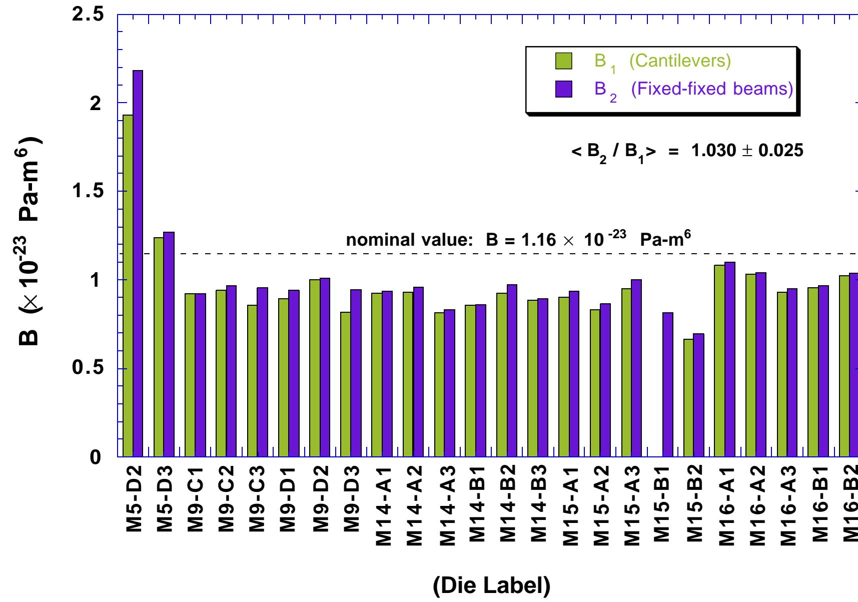

Figure 4.16: Tabulated B_1 and B_2 values of MUMPs cantilevers and fixed-fixed beams on the same die for various dies show excellent agreement. The large differences in the nominal B and measured B's reflects variations in geometry, where, for example, the MUMPs 5 D2 die has a $t \times g_o$ product which is approximately 20% higher than the nominal value of tg_o equal to $2.00 \times 2.07\ \mu\text{m}^2$, based on a constant E. The systematic difference in B_1 and B_2 suggests a residual modeling error.

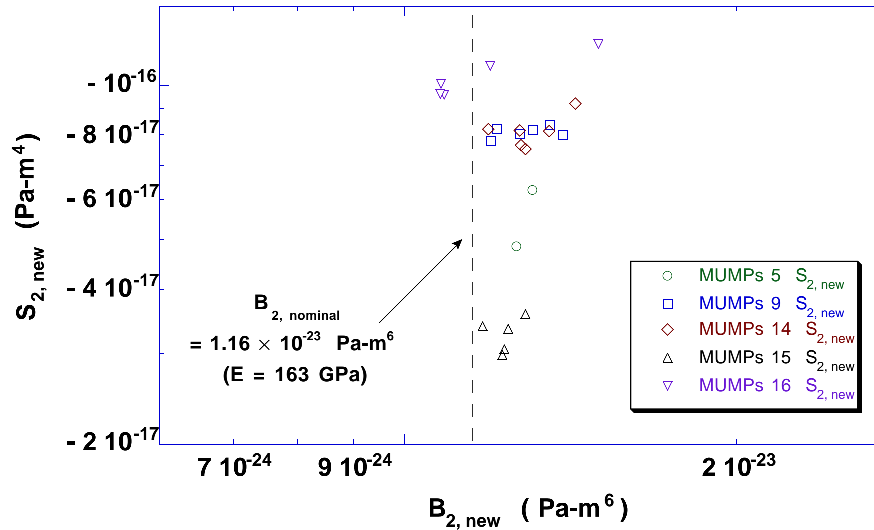

Figure 4.17: Elimination of correlated variations in t and g_o in the B_2's from Figure 4.15 tighten the distribution in the new B_2 values. The systematically larger value of the new B_2 values compared to the nominal value suggests a small scaling problem in the measured geometry.

CHAPTER 5

Discussion and Conclusions

The dependence of crystalline silicon's Young's modulus with orientation is well-known (Appendix A). It varies from a minimum of 130 GPa in the [100] direction to 188 GPa in the [111] direction. In the presence of strong texture normal to a random in-plane grain orientation, the effective in-plane modulus can vary from approximately 147 GPa for <100> out-of-plane textured polysilicon to 169 GPa for <111> textured polysilicon.

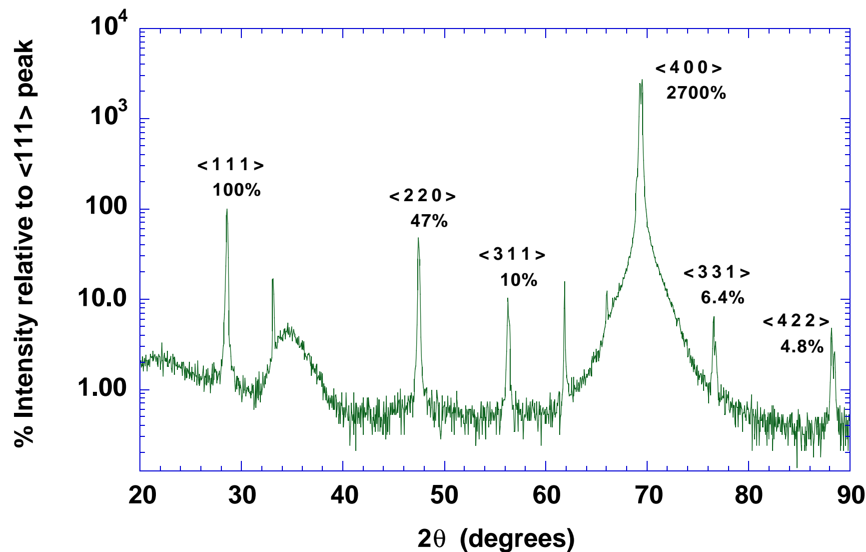

Figure 5.1: Theta-2Theta X-ray crystallographic data of 2 μm thick polysilicon layer from MUMPs 16. The large <400> peak is due to the silicon substrate. Relative peak intensities can be compared to expected values from a silicon powder diffraction standard in Table 5.1.

Completely untextured polysilicon has an effective isotropic modulus of approximately 163 GPa.

X-ray θ-2θ and pole figure crystallographic data from a recent MUMPs test wafer reveal no strong texture in the highly columnar polysilicon grains, either normal to the film, or in-plane [71]. The x-ray θ-2θ data is shown in Figure 5.1. For comparison, the θ-2θ silicon powder diffraction peak distribution, which is representative of untextured polysilicon, is listed in Table 5.1.

Silicon Powder Diffraction Standard (5-0565A) CuKα1 (λ = 1.5405 Å)			
d (Å)	**% Relative Intensity**	**<hkl>**	**2θ (degrees)**
3.1380	**100**	**111**	**28.41791**
1.9200	**60**	**220**	**47.30292**
1.6380	**35**	**311**	**56.09951**
1.3570	**8**	**400**	**69.16779**
1.2460	**13**	**331**	**76.36643**
1.1083	**17**	**422**	**88.05177**
1.0450	**9**	**511**	**94.96676**
0.9599	**5**	**440**	**106.7251**
0.9178	**11**	**531**	**114.1189**
0.8586	**9**	**620**	**127.5589**
0.8281	**5**	**533**	**136.9137**
Bragg condition: nλ = 2d sinθ, n = 1, 2, 3 ...			

Table 5.1: Power diffraction standard representative of untextured polysilicon [72].

The theoretical calculations and x-ray data for polysilicon serve as a reference in comparing extracted polysilicon modulus values from various reported mechanical measurements, including M-TEST. These values are compiled in Table 5.2. The M-TEST results for both the MUMPs 5 and the averaged data from multiple MUMPs runs lie within 10% of the untextured polycrystalline modulus average of silicon.

Method	Property	Value	Composition	Reference
M-TEST	***E***	**155 ± 10 GPa***	**PSG-doped 580C LPCVD**	**Gupta, [21]**
		178 ± 3 GPa**		**Gupta, Ph.D.**
Tensile Strength	***E***	**169 ± 6 GPa*****	**PSG-doped 580C LPCVD**	**Sharpe, [47]**
Resonant Comb-Drives	***E***	**143 ± 7 GPa**	***in-situ* P-doped 560-610C**	**Beibl, [39]**
		168 ± 7 GPa	**PSG-doped 610C LPCVD**	
		150 ± 20 GPa	**PSG-doped 605C LPCVD**	**Tang, [36]**
Membrane Deflection	$E/(1-\nu^2)$	**162 ±** 3^{+} **GPa**	**undoped 620C LPCVD**	**Maier-Schneider, [46]**
Vertical Beam Resonance	***E***	**166 ±** 3^{+} **GPa**	**B-implanted 590C LPCVD**	**Tilmans, [31]**
		175 ± 21 GPa	**undoped 580C LPCVD**	**Guckel, [30]**

Table 5.2: Polysilicon mechanical properties reported in current literature.

*Data taken from a single MUMPs 5 die using a Dektak 8000.

** Data reported in thesis averaged over MUMPs 5, 9, 14, 15, and 16 using a Dektak IIA.

***Data averaged over MUMPs 6, 8, 10, 11, and 12.

The M-TEST modulus data in Table 5.1 was determined using two different Dektak machines. While the Dektak 8000 was calibrated and shown to behave consistently from day to day, the other Dektak IIA showed internal drift which could not be removed and varied in measurements by up to ± 5% from day to day. Therefore, while the precision of the data (B) is accurate to less than 2% for the multiple-run M-TEST data, the absolute accuracy of the conversion from B to E is limited by Dektak calibration drifts, which for the single MUMPs 5 measurement was less than ± 7%, but in the multiple-run measurement was about ± 20%. Similarly, the conversion error in S to $\sigma_o(1-\nu)$ for the multiple-run measurements is accurate to ± 13%.

Note, Sharpe reports on average a systematically higher modulus value than the 163 GPa polycrystalline average for the same polysilicon fabrication process tested with

M-TEST. Although Sharpe's tensile strength data are sensitive to only the first power in the film thickness, his results do not include an independent measurement of geometry from run to run [76]. Instead, nominal values stated by the fabrication facility are assumed, and correlated errors due to geometry are not removed. Figures 4.15 and 4.16 suggests that the relative variation of the polysilicon thickness and gap is as large as 20%. Such variation also places a large error on the absolute accuracy of Sharpe's data. Clearly, for both M-TEST and tensile strength measurements unknown geometry is a big problem.

5.1 Future Work and Applications

M-TEST can be improved in four areas. First, a better understanding of charging dielectrics, for example, the silicon nitride used in the MUMPs process, will reduce errors in the electrostatic force associated in the effective gap approximation derived from summing the free space gap to the dielectric thickness, and will improve M-TEST models. Secondly, an electrostatic fringing-field correction for the added force at the tip of cantilevers will help to reduce the systematic discrepancy between extracted values of B_1 and B_2. Thirdly, for routine thickness and gap measurements, either optical interference techniques or better calibration of the Dektak surface profilometer will be needed. And finally, understanding electromechanical behavior in the presence of etch holes, used in the release of surface-micromachined circular diaphragms, will allow Poisson's ratio extraction. Research in the last area is currently under progress using a Texas Instruments process, where aluminum diaphragms are fabricated with a timed-etch release, as shown in Figure 3.1 [70].

M-TEST structures also show potential for use as *in-situ* packaging strain sensors, as illustrated by their sensitivity to externally applied stress in Figure 4.12. Recent work has also shown that dynamic actuation of these devices can be used for *in-situ* leak monitoring of hermetically-sealed sensors or IC's [1].

5.2 Conclusions

The general M-TEST methodology is presented. Its sources of error are identified and then quantified wherever possible. Examples demonstrating M-TEST for use as a quality control monitor for geometry and for mechanical property extraction in the presence of residual stress are reported. Techniques for reducing M-TEST to practice are discussed.

As shown in this thesis, M-TEST's high sensitivity to geometry can be a limitation if the user is interested in mechanical property extraction, or an advantage if process monitoring of geometry is desired. Except for the tensile strength test, all other mechanical property extraction techniques including M-TEST in Table 5.2 require bending, and therefore are highly sensitive to errors in thickness measurements. M-TEST additionally requires a measurement of gap, whose error sensitivity scales similarly to the error in thickness. So while the modeling errors are small (~ 3% based on agreement between cantilevers and fixed-fixed beams) and the precision of the extraction of B and S from measured pull-in voltages are also small (~ 2%), the absolute accuracy of the M-TEST extracted mechanical properties E and $\sigma_o(1-\nu)$ is large (~ 20%), because of its vulnerability to the errors in the existing techniques for measuring geometry. Fixing this last issue is a new area of investigation.

Nevertheless, M-TEST is found to be a powerful technique because it allows *in-situ* measurements of mechanical properties and monitoring of geometry, by using *simple* test structures which can be part of *almost any* MEMS fabrication process and is *very easy* to instrument. In these regards, M-TEST is unique from all the other techniques mentioned in Table 5.2.

References

[1] R. K. Gupta and S. D. Senturia, "Pull-in Time Dynamics as a Measure of Absolute Pressure", *Tenth IEEE International Workshop on MEMS 1997*, Nagoya, JAPAN, January 26-30, 1997, pp. 290-294.

[2] L. Parameswaran, A. Mirza, W. K. Chan, and M. A. Schmidt, "Silicon Pressure Sensors Using a Wafer-bonded Sealed Cavity Process", *Proceedings of Transducers' 95 • Eurosensors IX, Volume 2*, Stockholm, SWEDEN, June 25-29, 1995, pp. 582-585.

[3] W. H. Ko, Q. Wang, and Y. Wang, "Touch Mode Capacitive Pressure Sensors for Industrial Applications", *Proceedings of the 1996 Solid-State Sensor and Actuator Workshop*, Hilton Head, SC, June 3-6, 1996, pp. 244-248.

[4] D. W. Burns, J. D. Zook, R. D. Horning, W. R. Herb, and H. Guckel, "A Digital Pressure Sensor Based on Resonant Microbeams", *Proceedings of the 1994 Solid-State Sensor and Actuator Workshop*, Hilton Head, SC, June 13-16, 1994, pp. 221-224.

[5] C. H. Mastrangelo and R. S. Muller, "Fabrication and Performance of a Fully Integrated μ-Pirani Gauge with Digital Readout", *Proceedings of Transducers' 91*, San Francisco, CA, June 24-27, 1991, pp. 245-248.

[6] C. Lu, M. Lemkin, and B. E. Boser, "A Monolithic Surface Micromachined Accelerometer with Digital Output", *IEEE Journal of Solid-State Circuits*, **30**, No. 12 (1995), pp. 1367-1373.

[7] L. Spangler and C. J. Kemp, "A Smart Automotive Accelerometer with On-Chip Airbag Deployment Circuits", *Proceedings of the 1996 Solid-State Sensor and Actuator Workshop*, Hilton Head, SC, June 3-6, 1996, pp. 211-214.

[8] K. H.-L. Chau, S. R. Lewis, Y. Zhao, R. T. Howe, S. F. Bart, and R. G. Marcheselli, "An Integrated Force-Balanced Capacitive Accelerometer for Low-g Applications", *Proceedings of Transducers' 95 • Eurosensors IX, Volume 1*, Stockholm, SWEDEN, June 25-29, 1995, pp. 593-596.

[9] M. W. Putty and K. Najafi, "A Micromachined Vibrating Ring Gyroscope", *Proceedings of the 1994 Solid-State Sensor and Actuator Workshop*, Hilton Head, SC, June 13-16, 1994, pp. 213-220.

[10] J. Bernstein, S. Cho, A. T. King, A. Kourepenis, P. Marciel, and M. Weinberg, "A Micromachined Comb-Drive Tuning Fork Gyroscope", *Digest IEEE/ASME MEMS Workshop*, Ft. Lauderdale, FL, February 1993, pp. 143-148.

[11] A. Padmanabhan, H. D. Goldberg, K. S. Breuer, and M. A. Schmidt, "A Silicon Micromachined Floating-Element Shear-Stress Sensor with Optical Position Sensing by Photodiodes", *Proceedings of Transducers' 95 • Eurosensors IX, Volume 2*, Stockholm, SWEDEN, June 25-29, 1995, pp. 436-439.

[12] T. Pan, D. Hyman, M. Mehregany, E. Reshotko, and B. Willis, “Calibration of Microfabricated Shear Stress Sensors”, *Proceedings of Transducers’ 95 • Eurosensors IX, Volume 2*, Stockholm, SWEDEN, June 25-29, 1995, pp. 443-446.

[13] M. A. Schmidt, R. T. Howe, S. D. Senturia, and J. H. Haritonidis, *IEEE Transactions on Electron Devices*, **ED-35** (1988), pp. 750-757.

[14] R. Amantea, C. H. Knoelder, F. P. Pantuso, V. K. Patel, D. J. Sauer, and J. R. Tower, “An Uncooled IR Imager with 5 mKelvin NEDT”, *1997 IRIS Specialty Group Meeting on Passive Sensors*, Tuscon, AZ, 1997.

[15] R. B. Apte, F. S. A. Sandejas, W. C. Banyai, and D. M. Bloom, “Deformable Grating Light Valves for High Resolution Displays”, *Proceedings of the 1994 Solid-State Sensor and Actuator Workshop (Invited Paper)*, Hilton Head, SC, June 13-16, 1994, pp. 1-6.

[16] L. J. Hornbeck, “128 × 128 Deformable Mirror Device”, *IEEE Transactions on Electron Devices*, **ED-30**, (1983), p. 539.

[17] M.-A. Gretillat, P. Thiebaud, N. F. de Rooij, and C. Linder, “Electrostatic Polysilicon Microrelays Integrated with MOSFETs”, *Proceedings of MEMS 1994*, Oiso, JAPAN, January 1994, pp. 97-101.

[18] W. P. Taylor, M. G. Allen, and C. R. Dauwalter, “A Fully Integrated Magnetically Actuated Micromachined Relay, *Proceedings of the 1996 Solid-State Sensor and Actuator Workshop*, Hilton Head, SC, June 3-6, 1996, pp. 231-234.

[19] K. Wang and C. T.-C. Nguyen, “High-Order Micromechanical Electronic Filters”, *Tenth IEEE International Workshop on MEMS 1997*, Nagoya, JAPAN, January 26-30, 1997, pp 25-30.

[20] S. D. Senturia, “Mechanical Properties of Microsensor Materials: How to Deal with Process Dependencies”, *Material Research Society Symposium Proceedings*, **239** (1992), pp. 3-11.

[21] R. K. Gupta, P. M. Osterberg, and S. D. Senturia, “Material Property Measurements of Micromechanical Polysilicon Beams”, *Proceedings of SPIE 1996 Conference (Invited Paper): Microlithography and Metrology in Micromachining II*, Austin, TX, October 14-15, 1996, pp. 39-45.

[22] R. K. Gupta, C. H. Hsu, M. A. Schmidt and S. D. Senturia, “Monitoring Plasma Overetching of Wafer-Bonded Microstructures”, Proceedings of Transducers’ 1995, Volume 1, Stockholm, June 1995, pp. 269-72.

[23] P. M. Osterberg, R. K. Gupta, J. R. Gilbert, and S. D. Senturia, “Quantitative Models for the Measurement of Residual Stress, Poisson’s Ratio and Young’s Modulus Using Electrostatic Pull-in of Beams and Diaphragms”, *Proceedings of the 1994 Solid-State Sensor and Actuator Workshop*, Hilton Head, SC, June 1994, pp. 184-188.

[24] P. M. Osterberg and S. D. Senturia, “M-TEST: A Test Chip for MEMS Material Property Measurement using Electrostatically Actuated Test Structures”, *IEEE Journal of Microelectromechanics (MEMS)*, **6**, No. 2 (1997) pp. 107-118.

[25] H. C. Nathanson, W. E. Newell, R. A. Wickstrom, and J. R. Davis, Jr., “The Resonant Gate Transistor”, *IEEE Transactions on Electron Devices*, **ED-14**, No. 3, March 1967, pp. 117-133.

[26] R. T. Howe and R. S. Muller, “Polycrystalline Silicon Mechanical Beams”, *Journal of Electrochemical Society*, **130**, June 1983, pp. 1420-1423.

[27] Devices courtesy of David Koester and Karen Markus at the Microelectronics Center of North Carolina (MCNC), and fabricated by the Multi-User MEMS Processes (MUMPs), *http://mems.mcnc.org*.

[28] C. H. Hsu and M. A. Schmidt, “Micromachined Structures Fabricated Using a Wafer-Bonded Sealed Cavity Process”, *Proceedings of the 1994 Solid-State Sensor and Actuator Workshop*, Hilton Head, SC, June 13-16, 1994, pp. 151-155.

[29] K. E. Petersen, “Dynamic Micromechanics on Silicon: Techniques and Devices”, *IEEE Transactions on Electron Devices*, **ED-25** (1978), pp. 1241-1250.

[30] H. Guckel, D. W. Burns, H. A. C. Tilmans, D. W. DeRoo, and C. R. Rutigliano, “Mechanical Properties of Fine Grained Polysilicon, The Repeatability Issue”, *Proceedings of the IEEE Solid-State Sensors and Actuators Workshop*, Hilton Head, SC, June 1988, pp. 96-99.

[31] H. A. C. Tilmans, “Micro-Mechanical Sensors Using Encapsulated Built-in Resonant Strain Gauges”, Ph.D. Thesis, MESA Research Institute of the University of Twente, Enschede, The Netherlands, 1993.

[32] L. Kiesewetter, J.-M. Zhang, D. Houdeau, and A. Steckenborn, “Determination of Young’s Moduli of Micromechanical Thin Films Using the Resonance Method”, *Sensors and Actuators A*, **35** (1992) pp. 153-159.

[33] H. Okada, K. Suzuki, and T. Kuriyama, “Measurement of Young’s Modulus, Residual Stress, and Air Damping Effects Using Silicon Microstructures”, *Sensors and Materials*, **4**, No. 5 (1993) pp. 239-249.

[34] R. Schellin, G. Heß, W. Kühnel, C. Thielemann, D. Trost, J. Wacker, and R. Steinmann, “Measurements of the Mechanical Behavior of Micromachined Aluminized Silicon and Silicon Nitride Diaphragms”, *Sensors and Materials*, **7**, No. 5 (1995) pp. 347-360.

[35] L. M. Zhang, D. Uttamchandani, and B. Culshaw, “Measurement of the Mechanical Properties of Silicon Resonators”, *Sensors and Actuators A*, **29** (1991) pp. 79-84.

[36] W. C. Tang, “Electrostatic Comb Drive for Resonant Sensor and Actuator Applications”, Ph.D. Thesis, University of California at Berkeley, 1990.

[37] R. I. Pratt, G. C. Johnson, R. T. Howe, and D. J. Nikkel, Jr., "Characterization of Thin Films Using Micromechanical Structures", *Materials Research Society Symposium Proceedings*, **276** (1992) pp. 197-202.

[38] H. Kahn, S. Stemmer, K. Nandakumar, A. H. Heuer, R. L. Mullen, R. Ballarini, and M. A. Huff, "Mechanical Properties of Thick, Surface Micromachined Polysilicon Films", *Proceedings IEEE MEMS 1996*, San Diego, CA, February 11-15, 1996, pp. 343-348.

[39] M. Biebl, G. Brandl, and R. T. Howe, "Young's Modulus of *in-situ* Phosphorus-doped Polysilicon", *Proceedings of Transducers' 1995, Volume II*, Stockholm, SWEDEN, June 1995, pp. 80-83.

[40] Q. Zou, Z. Li, and L. Liu, "New Methods for Measuring Mechanical Properties of Thin Films in Micromachining: Beam Pull-in Voltage (V_{PI}) Method and the Long Beam Deflection (LBD) Method", *Sensors and Actuators A*, **48** (1995), pp. 137-143.

[41] H. Guckel, D. W. Burns, C. Visser, H. A. C. Tilmans, and D. DeRoo, "Fine-grained Polysilicon Films with Built-in Tensile Strain", *IEEE Transactions on Electron Devices*, **35** (1988), pp. 800-801.

[42] B. P. van Drieënhuizen, J. F. L. Goosen, P. J. French, and R. F. Wolffenbuttel, "Comparison of Techniques for Measuring Both Compressive and Tensile Stress in Thin Films", *Sensors and Actuators A*, **37-38** (1993) pp. 756-765.

[43] S. Wang, S. Crary, and K. Najafi, "Electronic Determination of the Modulus of Elasticity and Intrinsic Stress of Thin Films using Capacitive Bridges", *MRS Symposium Proceedings*, **276** (1992), pp. 203-208.

[44] J. Å. Schweitz, "Mechanical Characterization of Thin Films by Micromechanical Techniques", *MRS Bulletin*, July 1992, pp. 34-45.

[45] K. Najafi and K. Suzuki, "A Novel Technique and Structure for the Measurement of Intrinsic Stress and Young's Modulus of Thin Films", *Proceedings of MEMS 1989*, Salt Lake City, February 1989, pp. 96-97; K. Najafi and K. Suzuki, "Measurement of Fracture Stress, Young's Modulus, and Intrinsic Stress of Heavily Boron-Doped Silicon Microstructures", *Thin Solid Films*, **181** (1989), pp. 251-258.

[46] D. Maier-Schneider, A. Ersoy, J. Maibach, D. Schneider, and E. Obermeier, "Influence of Annealing on Elastic Properties of LPCVD Silicon Nitride and LPCVD Polysilicon", *Sensors and Materials*, **7**, No. 2 (1995) pp. 121-129.

[47] W. N. Sharpe, Jr., B. Yuan, R. Vaidyanathan, and R. L. Edwards, "New Test Structures and Techniques for Measurement of Mechanical Properties of MEMS Materials (Invited Paper)", *Proceedings of SPIE 1996 Microlithography and Metrology in Micromachining II*, Austin, TX, October 1996, pp. 78-91; W. N. Sharpe, Jr., B. Yuan, R. Vaidyanathan, and R. L. Edwards, "Measurements of Young's Modulus,

Poisson’s Ratio, and Tensile Strength of Polysilicon”, *Tenth IEEE International Workshop on MEMS 1997*, Nagoya, JAPAN, January 26-30, 1997, pp. 424-429.

[48] H. J. McSkimin, “Measurement of Elastic Constants at Low Temperature by Means of Ultrasonic Waves - Data for Silicon and Germanium Single Crystals, and for Fused Silica”, *Journal of Applied Physics*, **24**, No. 8 (1953) pp. 988-997.

[49] H. D. Young, “Statistical Treatment of Experimental Data”, McGraw-Hill, 1962.

[50] H. B. Palmer, “The Capacitance of a Parallel-Plate Capacitor by the Schwartz-Christoffel Transformation”, *Electrical Engineering*, **56**, March 1937, pp. 363-366.

[51] F. R. Morgenthaler, “Theoretical Studies of Microstrip Antennas, Volume 1: General Design Techniques and Analyses of Single and Coupled Elements”, U.S. Department of Transportation, *Federal Aviation Administration Report No. FAA-EM-79-11, I*, September 1979.

[52] S. P. Timoshenko, “Theory of Plates and Shells”, McGraw-Hill, 1987, pp. 4-6, 118, 125.

[53] S. H. Crandall, N. C. Dahl, T. J. Lardner, R. R. Archer, “An Introduction to the Mechanics of Solids, Second Edition in SI Units”, McGraw-Hill, 1978.

[54] P. M. Osterberg, “Electrostatically Actuated Microelectromechanical Test Structures for Material Property Measurement”, Ph. D. Thesis, M.I.T., September 1995.

[55] MATLAB scripts are available by request from the author.

[56] T. A. Lober, J. Huang, M. A. Schmidt, and S. D. Senturia, “Characterization of the Mechanisms Producing Bending Moments in Polysilicon Micro-cantilever Beams by Interferometric Deflection Measurements”, *Proceedings of the 1988 IEEE Solid-State Sensor and Actuator Workshop*, Hilton Head, SC, June 6-9, 1988, pp. 92-95.

[57] R. L. Mullen, M. Mehregany, M. P. Omar, and W. H. Ko, “Theoretical Modeling of Boundary Conditions in Microfabricated Beams”, *Proceedings of IEEE Micro Electro Mechanical Systems (MEMS) 1991*, Nara, JAPAN, January 1991, pp. 154-159.

[58] G. Gerlach, A. Schroth, and P. Pertsch, “Influence of Clamping Conditions on Microstructure Compliance”, *Sensors and Materials*, **8**, No. 2 (1996) pp. 79-98.

[59] E. H. Yang and S. S. Yang, “A New Technique for the Quantitative Determination of the Stress Profile Along the Depth of *p+* Silicon Films”, *Proceedings of Transducers’ 1995, Volume 2*, Stockholm, SWEDEN, June 1995, pp. 68-71.

[60] R. Hill, “The Elastic Behaviour of a Crystalline Aggregate”, *Phys. Soc.* **A65** (1952) pp. 351-354.

[61] G. Simmons and H. Wang, “Single Crystal Elastic Constants and Calculated Aggregate Properties: A Handbook, 2nd Ed.”, MIT Press, Cambridge, Massachusetts, 1971, pp. 85, 262.

[62] E. H. Mansfield, “The Bending and Stretching of Plates”, Pergamon Press, 1964, pp. 3, 81, 99, 114-116, 122-133.

[63] P. M. Osterberg and S. D. Senturia, “MemBuilder: An Automated 3D Solid Model Construction Program for Microelectromechanical Structures”, *Proceedings of Transducers’ 95 • Eurosensors IX, Volume 2*, Stockholm, SWEDEN, June 25-29, 1995, pp. 21-24.

[64] Kaleidagraph 3.0 (Synergy Software) curve-fit routines and macro library for automated mechanical property extraction available from author by request.

[65] J. A. Gregory, D. J. Young, R. W. Mountain, and C. L. Doherty, Jr., “Characterization of Low Pressure Chemically Vapor Deposited Silicon Nitride Using Experimental Design”, *Thin Solid Films*, **206**, (1991), pp. 11-17.

[66] P. E. Bagnoli, A. Piccirillo, P. Valenti, G. Civale, and A. L. Gobbi, “Silicon Nitride / Semiconductor Interface State Density as a Function of the Insulator Stoichiometry”, *Applied Surface Science*, **56-58**, (1992), pp. 881-887.

[67] MEMS email discussion group. Archives searchable at URL: *http://mems.isi.edu*.

[68] L. V. Ngo, P. Nelson, and C.-J. Kim, “Surface-Micromachined Beams Without Spring Effect of Anchor Step-up”, *Proceedings of the 1996 Solid-State Sensor and Actuator Workshop*, Hilton Head, SC, June 3-6, 1996, pp. 140-143.

[69] J. R. Gilbert, R. Legtenberg, and S. D. Senturia, “3D Coupled Electro-mechanics for MEMS: Applications of CoSolve-EM”, *Proceedings of IEEE MEMS 1995*, Amsterdam, the Netherlands, February 1995, pp. 122-127.

[70] V. L. Rabinovich, R. K. Gupta, and S. D. Senturia, “The Effect of Release-Etch Holes on the Electromechanical Behavior of MEMS Structures”, *Transducers’ 97*, Chicago, IL, June 16-19, 1997, pp. 1125-1128.

[71] X-ray crystallographic measurements courtesy of Steve Seel, Department of Material Science and Engineering, M.I.T.

[72] C. S. Barrett and T. B. Swanson, “Structure of Metals: Crystallographic Methods, Principles, and Data, Third Edition”, Pergamon Press, 1980.

[73] J. D. Renton, “Applied Elasticity: Matrix and Tensor Analysis of Elastic Continua”, John Wiley & Sons, 1987.

[74] W. A. Brantley, “Calculated Elastic Constants for Stress Problems Associated with Semiconductor Devices”, *Journal of Applied Physics*, **44**, No. 1, (1973) pp. 534-535.

[75] Z. Hashin and S. Shtrikman, “On Some Variational Principles in Anisotropic and Nonhomogeneous Elasticity” & “A Variational Approach to the Theory of the Elastic Behaviour of Polycrystals”, *Journal Mech. and Phys. Solids*, **10**, (1962), pp. 335-342 & 343-352.

[76] Professor William N. Sharpe, Jr., John Hopkins University, private communication.

APPENDIX A

Silicon Mechanical Properties

The stiffness matrix [S] and compliance matrix [C] for a cubic crystal such as silicon are shown in equations (A.1) and (A.2). The principle stresses σ_{ii} and the principle strains ε_{ii} are along the crystal's three axes of symmetry, and σ_{ij} and ε_{ij} for $i \neq j$ are the shear stresses and shear strains, respectively [73].

$$[S]\{\sigma\} \equiv \begin{bmatrix} s_{11} & s_{12} & s_{12} & 0 & 0 & 0 \\ s_{12} & s_{11} & s_{12} & 0 & 0 & 0 \\ s_{12} & s_{12} & s_{11} & 0 & 0 & 0 \\ 0 & 0 & 0 & s_{44} & 0 & 0 \\ 0 & 0 & 0 & 0 & s_{44} & 0 \\ 0 & 0 & 0 & 0 & 0 & s_{44} \end{bmatrix} \begin{Bmatrix} \sigma_{11} \\ \sigma_{22} \\ \sigma_{33} \\ \sigma_{12} \\ \sigma_{13} \\ \sigma_{23} \end{Bmatrix} = \begin{Bmatrix} \varepsilon_{11} \\ \varepsilon_{22} \\ \varepsilon_{33} \\ \varepsilon_{12} \\ \varepsilon_{13} \\ \varepsilon_{23} \end{Bmatrix} \tag{A.1}$$

$$[C]\{\varepsilon\} \equiv \begin{bmatrix} c_{11} & c_{12} & c_{12} & 0 & 0 & 0 \\ c_{12} & c_{11} & c_{12} & 0 & 0 & 0 \\ c_{12} & c_{12} & c_{11} & 0 & 0 & 0 \\ 0 & 0 & 0 & c_{44} & 0 & 0 \\ 0 & 0 & 0 & 0 & c_{44} & 0 \\ 0 & 0 & 0 & 0 & 0 & c_{44} \end{bmatrix} \begin{Bmatrix} \varepsilon_{11} \\ \varepsilon_{22} \\ \varepsilon_{33} \\ \varepsilon_{12} \\ \varepsilon_{13} \\ \varepsilon_{23} \end{Bmatrix} = \begin{Bmatrix} \sigma_{11} \\ \sigma_{22} \\ \sigma_{33} \\ \sigma_{12} \\ \sigma_{13} \\ \sigma_{23} \end{Bmatrix} \tag{A.2}$$

The stiffness coefficients s_{ij}, and compliance coefficients c_{ij}, obtained from McSkimin [48], for crystal silicon are listed below.

$$s_{11} = 0.7681 \quad s_{12} = -0.2138 \quad s_{44} = 1.2559 \quad (\times 10^{-11}\ Pa^{-1}) \tag{A.3}$$

$$c_{11} = 1.6578 \quad c_{12} = 0.6394 \quad c_{44} = 0.7962 \quad (\times 10^{11}\ Pa) \tag{A.4}$$

For an arbitrary crystallographic direction, E can be calculated as shown in equation (A.5).

$$E = \left\{ s_{11} - 2\left(s_{11} - s_{12} - \frac{s_{44}}{2} \right)\left[l_1^2 l_2^2 + l_1^2 l_3^2 + l_2^2 l_3^2 \right] \right\}^{-1} \quad (A.5)$$

where, the l_i's are the direction cosines referred to the [100] direction. For example, l_1 equals $sin(\theta)\ cos(\phi)$, l_2 equals $sin(\theta)\ sin(\phi)$, and l_3 equals $cos(\theta)$, in a right-handed spherical coordinate system, where θ is the angle between the vector and the z-axis, and ϕ is the angle in the x-y plane between the in-plane vector components and the x-axis. A three dimensional contour of E in the arbitrary crystalline directions of silicon is shown in Figure A.1. Silicon's Young's modulus in selected orientations is given below.

$$E_{min} = E_{[100]} = 130.2\ GPa \qquad E_{[110]} = 169.2\ GPa \qquad E_{max} = E_{[111]} = 187.9\ GPa \quad (A.6)$$

Note, for all directions in the <111> plane, E is isotropic, and equals 169.2 GPa. The Poisson's ratio in a direction m orthogonal to l, is given below [74].

$$\upsilon = -\frac{s_{12} + \left(s_{11} - s_{12} - \frac{s_{44}}{2} \right)\left(l_1^2 m_1^2 + l_2^2 m_2^2 + l_3^2 m_3^2 \right)}{s_{11} - 2\left(s_{11} - s_{12} - \frac{s_{44}}{2} \right)\left(l_1^2 l_2^2 + l_1^2 l_3^2 + l_2^2 l_3^2 \right)} \quad (A.7)$$

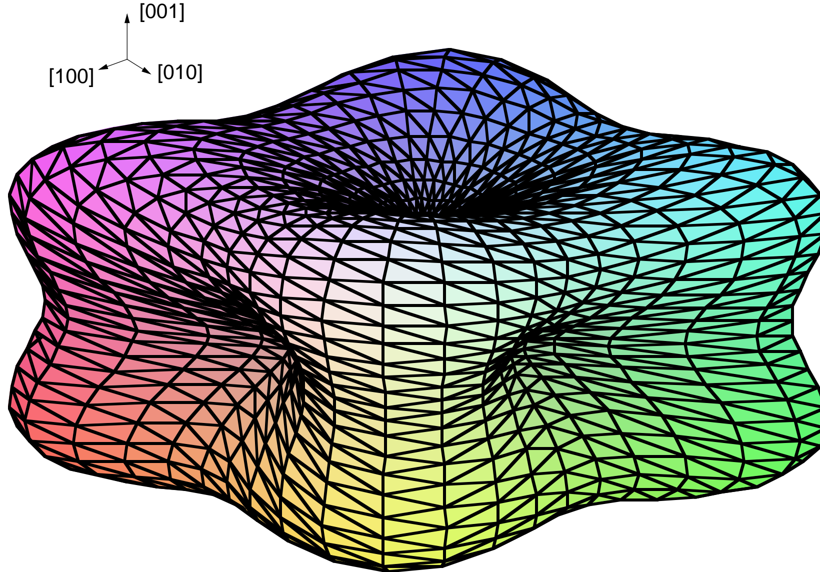

Figure A.1: Exaggerated spherical contour plot showing crystalline silicon's Young's modulus as a function of vector direction.

Note, the denominator term of equation (A.7) equals *1/E*. Also, observe that ν, like E, is isotropic in the <111> plane, and that $E/(1-\nu)$ is isotropic in the <100> plane, even though E and ν are not, and equals $1/(s_{11}+s_{12})$ [74].

The Reuss-Voight-Hill [60] theory calculates lower and upper bounds, based on random grain orientations in either uniform stress (Reuss) or uniform strain (Voight), for the effective isotropic modulus of randomly oriented grains of an anisotropic material. Reuss' method effectively averages the s_{ij}'s, and Voight's, the c_{ij}'s. For polycrystalline silicon, i.e. polysilicon, the results are summarized from [61], where E_R equals 159.6 GPa and E_V equals 165.9 GPa. The Poisson's ratio in these limits, ν_R and ν_V, equal 0.217 and 0.228. Reference [61] further lists tighter lower and upper bounds based on an improved theory [75] to give 162.6 GPa and 163.1 GPa, respectively.

An estimate of the effective in-plane isotropic modulus for a specific out-of-plane grain orientation, but a random, in-plane orientation, is determined from the average of the orientational dependent value of either E or $1/E$ from equation (A.5). This average is also calculated for the Poisson's ratio from equation (A.7). Averaged values for selected planes are shown in Table A.1, below.

Plane Orientation <hkl>	**Average Modulus In-Plane from [*E*]**	**Average Modulus In-Plane from [*1/E*]**	**Average In-Plane Poisson's Ratio ν**
<100>	147.1 GPa	148.4 GPa	0.177
<110>	163.1 GPa	165.5 GPa	0.239
<111>	169.2 GPa		0.262
<210>	157.0 GPa	158.6 GPa	0.214
<211>	163.1 GPa	163.9 GPa	0.238
<310>	152.5 GPa	153.8 GPa	0.197
<311>	156.8 GPa	157.8 GPa	0.214
<321>	163.1 GPa	164.3 GPa	0.238

Table A.1: Average silicon modulus and Poisson's ratio calculated for select plane cross sections centered at the origin of Figure A.1.

APPENDIX B

Microscope Stage Design

Top view:

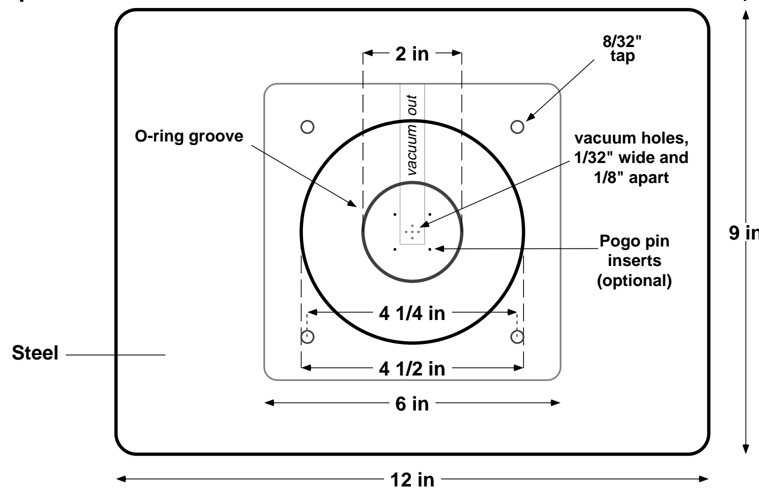

Side view:

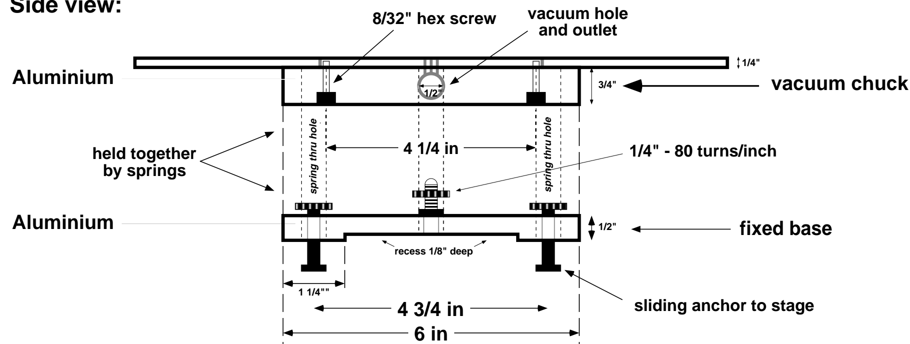

Bottom view:

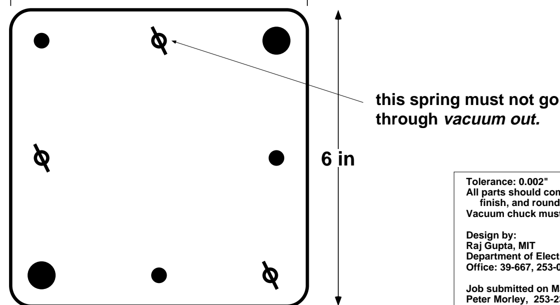

Tolerance: 0.002"
All parts should come with a polished finish, and rounded corners.
Vacuum chuck must be optically flat.

Design by:
Raj Gupta, MIT
Department of Electrical Engineering
Office: 39-667, 253-0726

Job submitted on May 9, 1995:
Peter Morley, 253-2392, FAX: 258-6158
LNS Machine Shop, MIT

APPENDIX C

Multilayer Test Structures

For a two-layer beam cross-section shown below,

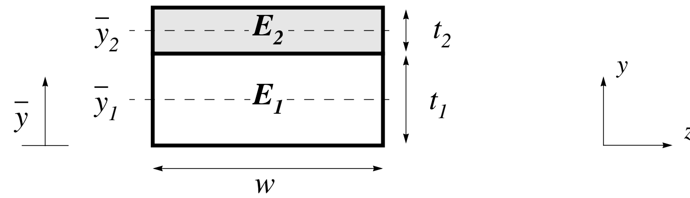

Figure C.1: Bilayer beam cross-section. Bottom layer has Young's modulus E_1 and thickness t_1, and top layer has E_2 and t_2. y_1 and y_2 are the respective locations of their neutral surfaces. y_N (not shown) is the neutral surface location of the bilayer structure. The beam has a length L, and it is electrostatically actuated over a nominal gap g_o.

the neutral surface location is given by,[1]

$$\bar{y}_N = \frac{E_1\bar{y}_1A_1 + E_2\bar{y}_2A_2}{E_1A_1 + E_2A_2}, \tag{C.1}$$

where $\bar{y}_1$ and $\bar{y}_2$ are the neutral surface locations and A_1 and A_2 are the cross-sectional areas of each individual layer. In terms of E_1, E_2, w, t_1, and t_2, the neutral plane $\bar{y}_N$ for the composite rectangular cross-section in Figure C.1 can be expressed as,

$$\bar{y}_N = \frac{E_1t_1^2 + E_2t_2^2 + 2E_2t_1t_2}{2(E_1t_1 + E_2t_2)}. \tag{C.2}$$

1. Stephen H. Crandall, Norman C. Dahl, and Thomas J. Lardner, "An Introduction to the Mechanics of Solids, Second Edition with SI Units", McGraw-Hill, Inc., 1978, pp. 430-431, 477, 495, 499.

From the parallel-axis theorem, the moment of area for the bilayer structure is,

$$I_{zz} = \sum_i I_{zz_i} + (\bar{y}_i - \bar{y}_N)^2 A_i \quad \text{where,} \quad I_{zz_i} = \frac{1}{12} w t_i^3 . \tag{C.3}$$

Similarly, the effective bending parameter B is,

$$B = \sum_i B_i + 12\,\tilde{E}_i (\bar{y}_i - \bar{y}_N)^2 t_i g_o^3 , \quad \text{where,} \quad B_i = \tilde{E}_i t_i^3 g_o^3 \tag{C.4}$$

and $\tilde{E}_i$ is the Young's modulus E_i for beams, which are narrow relative to their thickness and length, and the plate modulus $E_i/(1-\nu_i^2)$ for wide beams and circular diaphragms. In general, because the ν_i's will vary, $\bar{y}_N$ should be recalculated depending on structure type and dimensions. This will moderately affect expressions (C.1), (C.2), and (C.3). Note, for bilayered circular diaphragms, $\bar{y}_N$ can be recalculated by replacing E_i by $E_i/(1-\nu_i^2)$ in equations (C.1) and (C.2).

For bilayered structures like the one shown in Figure C.1, equation (C.4) evaluates to the following.

$$B = \tilde{E}_1 t_1 g_o^3 \left\{ t_1^2 + 3t_2^2 \left[\frac{1 + \frac{t_1}{t_2}}{1 + \frac{E_1 t_1}{E_2 t_2}} \right]^2 \right\} + \tilde{E}_2 t_2 g_o^3 \left\{ t_2^2 + 3t_1^2 \left[\frac{1 + \frac{t_2}{t_1}}{1 + \frac{E_2 t_2}{E_1 t_1}} \right]^2 \right\} \tag{C.5}$$

Cantilevers fabricated from films with in-plane (x-z) biaxial stress $\sigma(y)$ varying through the film thickness, have a zero net, thickness-averaged, biaxial stress ($\bar{\sigma}_x = \bar{\sigma}_z = S = 0$) when their thermal stresses from cooling relax after release.

In general, after cooling and release, fixed-fixed beams have a non-zero thickness-averaged axial stress $\bar{\sigma}_x$, but a zero $\bar{\sigma}_z$. In this case, the stress parameter S, for $w \gg (t_1+t_2)$,[1]

1. In this limit, both layers experience similar changes in strain ($\Delta\varepsilon_{z1} \approx \Delta\varepsilon_{z2}$) along the width after release.

equals $\overline{\sigma}_x(t_1+t_2)g_o{}^3$, where $\overline{\sigma}_x(t_1+t_2)$, in terms of $\overline{\sigma}$, the thickness-averaged value of $\sigma(y)$, is approximately,[1]

$$\overline{\sigma}_x(t_1+t_2) \approx \frac{\nu_1\nu_2(1-\nu_2)\left(1+\frac{E_2t_2}{E_1t_1}\right)-\left(1+\frac{E_2t_2}{E_1t_1}-\nu_2^2\right)\left(\frac{E_2}{E_1}+\frac{t_1}{t_2}\right)[1-\nu_1]}{\nu_1^2\nu_2^2\frac{E_2}{E_1}-\left(1-\nu_2^2+\frac{E_2t_2}{E_1t_1}\right)\left((1-\nu_1^2)\frac{E_2}{E_1}+\frac{t_1}{t_2}\right)}\,\overline{\sigma}t_1 + \frac{\nu_1\nu_2(1-\nu_1)\left(1+\frac{E_1t_1}{E_2t_2}\right)-\left(1+\frac{E_1t_1}{E_2t_2}-\nu_1^2\right)\left(\frac{E_1}{E_2}+\frac{t_2}{t_1}\right)[1-\nu_2]}{\nu_1^2\nu_2^2\frac{E_1}{E_2}-\left(1-\nu_1^2+\frac{E_1t_1}{E_2t_2}\right)\left((1-\nu_2^2)\frac{E_1}{E_2}+\frac{t_2}{t_1}\right)}\,\overline{\sigma}t_2\,. \tag{C.6}$$

As noted, the approximation in (C.6) ignores the adjustment in axial stress, when $w \sim t$, due to curvature ($\Delta\varepsilon_{z1} \neq \Delta\varepsilon_{z2}$) along the fixed-fixed beam width when a nonuniform stress-distribution through the film thickness causes $\overline{M}_{bx}$ to be nonzero before release.

Clamped circular diaphragms maintain a biaxial stress state after release, and their S equals $\sigma(t_1+t_2)g_o{}^3$.

The released cantilever is subject to a bending moment per unit length M_b along its length and width which cause its x-z plane to curl into a spherical shape. The bending moment equals,

$$M_b = -\int_0^{(t_1+t_2)} \sigma(y)\,[y-\bar{y}_N]\,dy\,. \tag{C.7}$$

The spherical curvature has a radius R_c along the cantilever's x- and z-axes of,[2]

$$R_c = \frac{E_1t_1}{(1-\nu_1)M_b}\left\{\frac{t_1^2-3t_1\bar{y}_N+3\bar{y}_N^2}{3}\right\} + \frac{E_2t_2}{(1-\nu_2)M_b}\left\{\frac{(t_2^2+3t_1t_2+3t_1^2)-6t_1\bar{y}_N-3t_2\bar{y}_N+3\bar{y}_N^2}{3}\right\}, \tag{C.8}$$

---

1. for other examples, see N. I. Muskhelishvili, “Some Basic Problems of the Mathematical Theory of Elasticity”, Fourth Corrected and Augmented Edition, Moscow 1954, translated from Russian by J. R. M. Radok, P. Noordhoff Ltd., Groningen, The Netherlands, 1963, Chapters 22, 24, 25.
2. see for reference, J. P. Den Hartog, “Advanced Strength of Materials”, Dover Publications, Inc., New York, 1952, pp. 106-112.

except for a small distance, typically 2× the width w,[1] from the fixed end, where the magnitude of R_c will be larger due to plate effects.

If $\sigma(y)$ equals zero for $0 \le y \le t_1$ and is uniformly biaxial σ_2 for $t_1 < y \le (t_1 + t_2)$, M_b evaluates to the following expression.

$$M_b = -\sigma_2 t_2 \left\{ t_1 \left[1 - \frac{1}{2}\left(1 + \frac{E_2 t_2}{E_1 t_1}\right)^{-1} \right] + \frac{t_2}{2}\left[1 - \frac{E_2}{E_1}\left(\frac{2 + \frac{t_2}{t_1}}{\frac{E_1}{E_2} + \frac{t_2}{t_1}} \right) \right] \right\} \quad \text{(C.9)}$$

Furthermore, for films where $t_2 \ll t_1$ and $E_1 \sim E_2$, the axial stress $\overline{\sigma}_x$ for fixed-fixed beams equals $\sigma_2 t_2(1\text{-}\nu_1)/(t_1+t_2)$, where σ_2 is the biaxial stress in the top film and ν_1 is the Poisson's ratio of the thick bottom film. Equations (C.5), (C.9) and (C.8) can also be simplified to the following, respectively.

$$B \approx E_1 t_1^3 g_o^3 + 3E_2 t_1^2 t_2 g_o^3 + 3E_1\left(\frac{E_2}{E_1}\right)^2 t_1 t_2^2 g_o^3 \approx [E_1 t_1 + 3E_2 t_2]\ t_1^2 g_o^3 \quad \text{(C.10)}$$

$$M_b \approx -\frac{\sigma_2 t_2}{2}\left\{ t_1\left[1 + \frac{E_2 t_2}{E_1 t_1}\right] + t_2\left[1 - \frac{E_2}{E_1}\right] \right\} \approx \frac{-\sigma_2 t_1 t_2}{2} \quad \text{(C.11)}$$

$$R_c \approx \frac{-E_1 t_1^3}{12(1-\nu_1)M_b} + \frac{E_2 t_1^2 t_2}{2M_b}\left[\frac{-(1+\nu_1)}{(1-\nu_2^2)} + \frac{1}{2}\right] \approx \frac{-E_1 t_1^3}{12(1-\nu_1)M_b} \quad \text{(C.12)}$$

Using M-TEST for $t_1 \gg t_2$, fitted values of B and R_c enable the extraction of $\sigma_2 t_2$ from cantilevers as shown by the following relation.

$$\sigma_2 t_2 \approx \frac{B}{6(1-\nu_1)R_c t_1 g_o^3} \quad \text{(C.13)}$$

Also, if E_1 is known, then E_2 can be extracted through algebra from the fitted value of B.

To improve the extraction sensitivity of σ_2 from thin films deposited on cantilevers, the length can be increased or the nominal gap can be reduced. This is seen directly from the

1. This general qualitative principle in elasticity is known as *St. Venant's principle*.

relation for f_c, the curvature adjustment factor for pull-in of cantilevers, shown below, which is second-power sensitive to length, and first-power sensitive to gap.

$$f_c \approx 1 - \frac{L^2 g_o^2 M_b}{2B} \tag{C.14}$$

Reducing the thickness t_1 decreases M_b and B, and improves sensitivity by the second-power of thickness. However, if $t_1 \sim t_2$, the simplifications in equations (C.10)-(C.13) become invalid, and the extraction procedure requires the use of equations (C.5), (C.9), and (C.8), directly. Note, that S from diaphragms and S from fixed-fixed beams can also be used to recheck the extracted value of σ_2.

Table C.1 shows calculations for pull-in voltages of typical cantilever geometries to be used in thin film stress measurements of copper deposited on polysilicon beams.

L (μm)	g_o (μm)	t_1 (μm)	t_2 (Å)	σ_2 (MPa)	$V_{PI, nominal}$ (V)	$\%\Delta V_{PI}$ $(f_c - 1)\times 100$
100	1	1	100	10	7.26	0.146
100	1	1	100	270	7.26	3.94
100	1	1	1600	10	8.45	~1.00
100	1	1	1600	270	8.45	~27.0
400	1	1	100	10	0.453	2.34
400	2	2	100	10	3.61	0.299
400	2	2	100	270	3.61	8.08
400	2	8	100	270	28.76	0.02
400	2	8	1600	270	29.34	7.50

Table C.1: Theoretically calculated values of V_{PI} for bilayered cantilevers made from unstressed polysilicon (E = 163GPa, $\sigma_1 = 0$) with thickness t_1, and an overlaying copper thin film (E = 117GPa) with thickness t_2 and biaxial stress of σ_2.